GTPase activating protein DLC1 spatio-temporally regulates Rho signaling

Max Heydasch[1,†], Lucien Hinderling[1,2,†], Jakobus van Unen[1], Maciej Dobrzynski[1], Olivier Pertz[1,*]

[1]Institute of Cell Biology, University of Bern, 3012 Bern, Switzerland

[2]Graduate School for Cellular and Biomedical Sciences, University of Bern, Switzerland

[†] These authors contributed equally to this work

[*] Corresponding author: olivier.pertz@unibe.ch

Abstract

Tightly regulated spatio-temporal Rho GTPase activity patterns regulate morphogenetic processes such as cell migration. Emerging evidence suggests that binding of Guanine nucleotide exchange factors (GEFs) and GTPase activating proteins (GAPs) to the cytoskeleton or adhesions mediate feedback regulation to spatio-temporal Rho GTPase activation. To explore such feedback regulation, we study the Rho specific GAP Deleted in Liver Cancer 1 (DLC1) which binds to focal adhesions (FAs) through mechanosensitive interactions. Using a FRET biosensor, we show that DLC1 loss of function leads to global increase in Rho activity and contractility throughout the cell without affecting a striking lamellar RhoA activity band in fibroblasts. To interrogate the Rho GTPase signaling flux, we build a genetic circuit consisting of an optogenetic actuator to control Rho activity, and a Rho activity biosensor. In spreading cells at steady state, optogenetic manipulation of Rho activity reveals that DLC1 controls the rate of Rho activation rather than duration, both at FAs and at the plasma membrane (PM). Local and reversible optogenetic control of contractility shows that DLC1 associates/dissociates with FAs during their reinforcement/relaxation. This might provide positive feedback that locally increases the rate of Rho activation at FAs that experience local tension to facilitate FA disassembly. Our results indicate that DLC1 operates both at the PM and at FAs to regulate global Rho activity levels at steady state, or to amplify local Rho activity at FAs experiencing a strong mechanical input, presumably to induce robust FA disassembly. This provides new insights in the complexity of spatio-temporal Rho GTPase signaling.

Introduction

Rho GTPases regulate the cytoskeletal dynamics that power morphogenetic processes at the cell- and tissue level (Etienne-Manneville and Hall, 2002). Their activity is tightly controlled in time and space by GEFs and GAPs, which respectively activate and inhibit Rho GTPases. In the GTP-loaded, active state, Rho GTPases bind downstream effectors that regulate cytoskeletal dynamics and other cellular processes. Based on classic experiments that include measuring population-averaged Rho GTPase activity levels, as well as overexpressing dominant positive/negative Rho GTPase mutants, it was proposed that Rac1 controls lamellipodial protrusion, Cdc42 regulates filopodium formation, and RhoA controls myosin-based contractility.

Recent studies in which spatio-temporal Rho GTPase activation dynamics were measured using fluorescence resonance energy transfer (FRET)-based biosensors, revealed a much higher signaling complexity. During cell migration, RhoA, Rac1 and Cdc42 are all activated in membrane protrusions at the leading edge (Itoh et al., 2002; Kraynov et al., 2000; Nalbant et al., 2004; Pertz et al., 2006). Further, the three Rho GTPases are activated in specific spatio-temporal sequences during the protrusion/retraction cycles that fluctuate on time and length scales of seconds and single micrometers (Machacek et al., 2009). A further level of complexity is that these Rho GTPase activity sequences vary depending on the cell system (Hu et al., 2022; Machacek et al., 2009; Martin et al., 2016). This indicates that complex spatio-temporal Rho GTPase signaling programs regulate processes such as cell migration. Similarly as for Ras GTPases (Schmick et al., 2015), it is now clear that these Rho GTPase signaling patterns most likely result from a precise spatio-temporal regulation of Rho GTPase signaling fluxes controlled by GEFs and GAPs (Bement and von Dassow, 2014; Fritz and Pertz, 2016; Pertz, 2010). In this signaling flux, specific GEFs will be locally activated to load Rho GTPases with GTP depending on different cellular inputs. These GTP-loaded GTPases will then subsequently diffuse in the plasma membrane by virtue of their C-terminal lipid moiety until they encounter a locally activated GAP which eventually deactivates them. The interplay of GEFs, GAPs and diffusion of Rho GTPases in the PM will ultimately lead to the formation of a Rho GTPase activity pattern. Modelling studies have suggested that sophisticated dynamic signaling behaviors can emerge from the interplay of GEFs, GAPs, and GTPases within a signaling network (Tsyganov et al., 2012). Steady-state images of Rho GTPase activity patterns do not provide information about the whole Rho GTPase flux mentioned above.

This signaling complexity is consistent with the large amount of GEFs and GAPs that are ubiquitously expressed in cells (Fusco et al., 2016, 2016; Moon and Zheng, 2003; Mosaddeghzadeh and Ahmadian, 2021; Müller et al., 2020; Rossman et al., 2005). Recently, a system-wide screen has revealed that many GEFs and GAPS localize to cytoskeletal structures as well as adhesion complexes such as focal adhesions (FAs)

(Müller et al., 2020). This strongly suggests the existence of feedback mechanisms from the cytoskeleton and FAs to Rho GTPase signaling. In this study, it was shown that Rac1-specific GEFs bind to FAs at the front, while Rac1-specific GAPs bind to FAs and at the back of the lamella of fibroblasts. This precise, asymmetric positioning of GEFs and GAPs might then regulate the Rho GTPase flux that produces the wide gradient of Rac activity observed at the leading edge of fibroblasts (Itoh et al., 2002; Kraynov et al., 2000; Martin et al., 2016). Such feedback regulation might allow leading edge Rac1 activity to constantly integrate mechanosensitive inputs from FAs, allowing dynamic regulation of Rac1 activity required to fine tune cell migration. Another prominent example of such spatio-temporal feedback regulation are the excitable RhoA activity patterns observed in the cortex during cytokinesis in *Xenopus Laevis* (Bement and von Dassow, 2014), that have also been observed in mammalian cells (Graessl et al., 2017). Here, RhoA activity waves that control F-actin wave patterns are spatially regulated by a RhoGAP that is locally regulated by F-actin (Bement et al., 2015a). Thus, cytoskeletal feedback to Rho GTPase regulation might be crucial to generate dynamic Rho GTPase signaling patterns. Understanding such spatio-temporal feedback regulation is not accessible with classic genetic approaches in which long term perturbation of Rho GTPases, their regulators and effectors rapidly result in a new mechanochemical state of the cell, that will not be informative about an initial signaling/mechanical state of interest (Isogai and Danuser, 2018). Further, it is currently unknown which specific features of spatio-temporal Rho GTPase signaling are regulated to produce signaling patterns. For example, does negative regulation by a GAP solely control Rho GTPase signal termination, or could it also modulate, less intuitive parameters such as the rate of activation? Tackling such questions requires new tools to acutely and transiently perturb the Rho GTPase flux to understand its spatio-temporal regulation, directly in single living cells. Note that this experimental paradigm was successful at analyzing the Mitogen activated protein kinase (MAPK network) (Blum et al., 2019; Dessauges et al., 2022; Ryu et al., 2015).

A promising candidate to investigate how mechanical feedback from FAs can spatio-temporally shape Rho GTPase activity is the RhoA-specific GAP Deleted in Liver Cancer 1 (DLC1). DLC1 has been shown to both bind the plasma membrane (PM) (Erlmann et al., 2009), as well as FAs (Haining et al., 2018; Kaushik et al., 2014). At the PM, interaction with phosphatidylinositol-4,5-bisphosphate (PI(4,5)P2) can regulate GAP activity (Erlmann et al., 2009). At the FA, DLC1 interacts with the r7-r8 domains of the FA protein talin in a mechanosensitive fashion (Gingras et al., 2008; Goult et al., 2021; Haining et al., 2018; Zhao et al., 2022), as well as with Focal adhesion kinase (Li et al., 2011). When talin is in a state of low mechanical strain, it binds to DLC1, and presumably leads to local RhoA inactivation. However, upon force application, the r7-r8 domains unfold leading to dissociation of DLC1 from talin, leading to loss of negative RhoA regulation. This suggests that DLC1 is regulated at FAs by mechanosensitive interactions, which can relay information about the mechanical state of the cell to control RhoA activity.

In this work, we explore the spatio-temporal regulation of RhoA activity by DLC1. We show that knocking out DLC1 in REF52 fibroblasts leads to increased amplitude in RhoA throughout the cell. This is accompanied by an increased contractility that augments FAs and stress fibers (SFs). To explore how DLC1 contributes to Rho GTPase activity fluxes, we built a genetic circuit consisting of an optogenetic actuator to activate Rho with light, and a spectrally compatible biosensor to measure Rho activity. Transient optogenetic recruitment of a Rho GEF domain at FAs or at the PM led to an increase in the rate of activation of Rho in *DLC1* KO versus WT cells at both subcellular localizations. However, we found that in both control and DLC1 null cells, RhoA activation was more efficient at FAs compared to the PM. Further, acute and local manipulation of contractility with the optogenetic actuator revealed that DLC1 dynamically associates/dissociates with FAs under acute mechanical tension/relaxation. Our results suggest a complex mechanism in which DLC1-dependent Rho regulation can occur both at the PM and at FAs, with a dependence on mechanosensitive signals on the latter.

Results

DLC1 deficient cells show increased formation of SFs and FAs

To investigate the function of DLC1 in cytoskeletal and adhesion dynamics, we knocked down (KD) DLC1 in rat REF52 fibroblasts via small interfering RNA (siRNA). We also created a knockout (KO) cell line via Crispr/Cas9, that has a frameshift deletion at position 841 of Exon 5 of the gene, resulting in an early in frame stop codon 100 bp downstream of the cut. Gene-editing was validated by sequencing the endogenous locus. We were unable to test expression levels using western blot because of the absence of commercially available antibodies specific for rat DLC1. We then also rescued the DLC1 KO cells with an mCherry-labeled DLC1 construct using stable transfection with a piggyBac transposase system. REF52 fibroblasts were seeded at subconfluent density onto fibronectin-coated glass bottom wells and allowed to spread for one hour before fixation, leading to an isotropic spreading state in control, wild-type (WT) cells. To assess the impact of DLC1 deficiency on the formation of cytoskeletal and adhesion structures, we stained for F-actin (phalloidin) and paxillin (Figure 1A) or phospho-myosin light chain (pMLC) (Figure 1B). Consistent with an expected increase in RhoA activity, we observed a phenotype of increased contractility as documented by increased lamella size, SF content, number of FAs, and increased pMLC. This increased contractility led to the loss of the isotropic spreading observed in WT cells. Rescue with the DLC1 construct reverted the cells to a less contractile phenotype that displayed a lamella of identical size as WT cells, enabling the characteristic isotropic spreading observed in WT cells. Quantification of these images revealed both an increase in lamella size (Figure 1C) and FA area (Figure 1D) in DLC1 KD and KO cells versus WT and rescue cells (Figure1C). As previously documented in

149 fibroblasts (Kaushik et al., 2014), these results indicate that DLC1 feeds into the regulation
150 of contractility, SF and FA formation in fibroblasts. The less penetrant phenotype observed
151 in KO versus KD suggests that the KO cells might be able to adapt to the long-term absence
152 of DLC1, while KD cells had less than 48 hours to adjust to the new mechanical
153 state. These experiments also validate the *DLC1* KO cells and *DLC1* KO rescued with
154 mCherry-DLC1 that will be used in subsequent experiments.

155

156 **DLC1 deficient cells display altered spreading dynamics, lack of polarization**
157 **and efficient migration**

158 We timelapsed REF52 WT and *DLC1* KO cells for multiple hours in presence of platelet
159 derived growth factor (PDGF), a potent stimulator of fibroblast motility (Martin et al., 2014),
160 and evaluated their ability to migrate. We found that *DLC1* KO cells displayed a reduction
161 in both their speed of migration and their ability to migrate directionally (Figure S1A-C). We
162 then investigated cytoskeletal dynamics during spreading using REF52 fibroblasts stably
163 expressing the F-actin marker LifeAct (Riedl et al., 2008). Imaging early spreading (e.g. 20
164 minutes after plating) revealed no clear differences in edge dynamics in WT versus *DLC1*
165 KO cells (Figure 2A). However, kymograph analysis clearly showed that the lamella that
166 characteristically starts directly at the leading edge of the highly contractile REF52 cells
167 (Martin et al., 2016, 2014), was wider in *DLC1* KO versus WT cells. Later, 1 hour after
168 plating, when the cells are still spreading, lamellipodial protrusion/retraction cycles of wider
169 amplitude were observed in *DLC1* KO versus WT cells (Figure 2B, Movie S1), with again
170 a large increase in SF content (Figure 2B, right panel). After initial spreading, REF52
171 fibroblasts break their symmetry and eventually display short episodes of polarized cell
172 migration. Later, contractility builds up leading cells with spindle-like morphology. This
173 process occurs on timescales of multiple hours. To capture these behaviors, we
174 investigated cytoskeletal dynamics over the next 10 hours after reseeding at a slower
175 timescale that precludes observation of lamellipodial dynamics. While WT cells efficiently
176 broke their symmetry, and could display short stretches of polarized migration, *DLC1* KO
177 cells displayed robust stress fibers that hampered symmetry breaking and polarization
178 (Figure 2C, Movie S2). *DLC1* KO cells therefore rapidly adopted a spindle-like shape.
179 Quantification of the adoption of such a spindle shape phenotype showed that WT cells will
180 assume the spindle-like shape much later than *DLC1* KO cells and often fail to do so
181 entirely within the 10 hours of imaging (Figure 2D). Further highlighting a role for DLC1 in
182 RhoA-mediated control of contractility, we found that DLC1 overexpression leads to strong
183 reduction in the number of SFs (Figure S2A). Together, these results show that DLC1 loss
184 of function leads to increased contractility at the onset of spreading, which later impedes
185 polarization and directional cell migration.

186

187 **DLC1 deficient cells display an increase in global RhoA activity, without any**
188 **marked differences in RhoA activity pattern**

189 To explore how DLC1 spatio-temporally controls RhoA activity, we used RhoA2G (Fritz et
190 al., 2013), a fluorescence resonance energy transfer (FRET)-based biosensor that reports
191 on RhoA activity together with the Lifeact F-actin marker during spreading. As previously
192 observed (Martin et al., 2014), a RhoA activity band that correlates with the lamellar
193 contractile actomyosin network of the cell can be observed at the cell edge of WT REF52
194 fibroblast (Figure 3A, Movie S3). In *DLC1* KO cells, we observed global elevation of RhoA
195 activity throughout the cell. Quantification of both the average activity per cell and the local
196 edge RhoA activity revealed increased RhoA activity (Figure 3B). Kymograph analysis
197 revealed that the lamellar RhoA activity band remained of constant size during spreading
198 (Figure 3A). Examining cells approximately 10 hours after spreading when they had fully
199 spread, and WT cells had adopted a more contractile state, the DLC1 *KO* cells still exhibited
200 a global increase in RhoA activity (Figure 3C,D). This increase was however less strong
201 than in spreading cells, most likely because of a higher state of contractility in WT well-
202 spread versus spreading cells. We also evaluated the effect of overexpression of an
203 mCherry-tagged DLC1 on RhoA activity (Figure S2B). We observed that mild DLC1
204 expression, that remains mostly bound to FAs and to the PM and does not compromise
205 cell morphology, leads to a decrease in global RhoA activity. Strong DLC1 expression that
206 leads to a large cytosolic pool of DLC1 further diminishes global RhoA activity but then
207 compromises cell morphology. Together, these results suggest that DLC1 signaling at the
208 PM and at FAs controls global levels of RhoA activity within cells, rather than controlling
209 the spatio-temporal RhoA activity pool observed at the lamella.

210

211 **Design of an optogenetic actuator - Rho biosensor to interrogate the Rho**
212 **GTPase flux**

213 While FRET measurements as shown above provide insight about a steady-state RhoA
214 activity pattern, they cannot probe in detail how a GEF/GAP/GTPase signaling network
215 might affect the Rho GTPase flux which most likely emerges from the regulation of multiple
216 GEFs and GAPs. For example, GAP-mediated negative regulation might control Rho
217 GTPase signal duration, but might also be involved in adjusting the rate of activation. We
218 reasoned that transient, acute optogenetic perturbations of the Rho GTPase flux, followed
219 by measuring Rho activity dynamics might provide new insights about its regulation. To
220 manipulate Rho activity in single living cells, we re-engineered an iLID-based optogenetic
221 actuator based on a DH/PH domain of the GEF LARG (Oakes et al., 2017) (Figure 4A). We
222 used a high affinity nano SspB domain for efficient light-dependent recruitment of the LARG
223 GEF domain to the iLID anchor. To better focus optogenetic activation, we also fused the
224 iLID anchor to a stargazin membrane anchor that slows down its diffusion (Natwick and

225 Collins, 2021). Both the stargazin-iLID anchor and the SspB-LARG domains were
226 separated by a P2A self-cleaving peptide, allowing for equimolar expression of both units
227 from a single operon. We refer to this construct as optoLARG. To interrogate the Rho
228 GTPase flux, we engineered a REF52 line that stably expressed the optogenetic construct
229 as well as a rhotekin-based G protein binding domain (rGBD) that reports on Rho activation
230 (Mahlandt et al., 2021). The rGBD probe is labelled with a tandem dimeric Tomato
231 (tdTomato) fluorophore that is spectrally orthogonal to optogenetic activation. We used a
232 truncated CMV promoter to warrant low expression level of the rGBD probe to avoid
233 dominant negative effects of the construct through inhibition of Rho signaling. We also
234 expressed a spectrally orthogonal far-red Lifeact-miRFP construct that reports on F-actin
235 dynamics. Because rGBD cannot distinguish between the activity of the RhoA, RhoB and
236 RhoC isoforms, we refer to any rGBD measurement as Rho activity. This is in marked
237 contrast with RhoA2G, the FRET biosensor we used above that is specific for RhoA (Fritz
238 et al., 2013), but is not spectrally compatible with optoLARG. Note that both biosensors are
239 able to measure active Rho GTPase pools during robust morphogenetic events such as
240 tail retraction (Fritz et al., 2013; Mahlandt et al., 2021), while rGBD misses leading edge
241 Rho GTPase activity pools widely observed using FRET probes (Machacek et al., 2009;
242 Martin et al., 2016; Pertz et al., 2006).

243 We then used a digital micromirror device (DMD) to spatially shine repetitive pulses of blue
244 light delivered at different frequencies on 2 distinct regions of interest (ROIs) at the edge
245 of fibroblasts. When light pulses were delivered at high frequency, we observed robust Rho
246 activation at the edge, which correlated with assembly of contractile F-actin structures and
247 potent edge retraction (Figure 4B, kymograph shown in 4C, Movie S4). Removal of the
248 blue light pulses led to a subsequent decrease in Rho activity, and reversion of the edge
249 to a protrusive state. Further, stimulating a ROI at the opposite edge of the cell with a lower
250 light pulse frequency led to a lower Rho activation, and less robust edge retraction. These
251 results indicate that depending on the strength of the light input, optoLARG can locally,
252 reversibly, and quantitatively control Rho activity in single living cells on timescales of
253 seconds, allowing us to acutely manipulate the Rho GTPase flux.

254

255 **Optogenetic interrogation of the Rho GTPase flux in WT and DLC1 KO cells**

256 Because DLC1 might both regulate the Rho GTPase flux both at the PM (Erlmann et al.,
257 2009) and at FAs (Haining et al., 2018), we performed a series of experiments using
258 optoLARG to transiently activate RhoA with the expectation of observing different
259 perturbations in Rho activity fluxes in control versus DLC1 KO cells. For that purpose, we
260 produced WT and *DLC1* KO REF52 lines expressing optoLARG, the tdTomato-rGBD
261 biosensor and miRFP-paxillin as a readout for focal adhesions. We first sought to locally
262 activate RhoA by illuminating large ROIs at edges and evaluate any difference in Rho

263 activity patterns using the spectrally compatible rGBD biosensor in WT versus *DLC1* KO
264 cells. We however were not able to identify a threshold optogenetic light input that would
265 induce different RhoA activity patterns and edge dynamics in WT versus the more
266 contractile *DLC1* KO cells. We observed that the same light input could induce edge
267 retraction in both WT and *DLC1* KO cells in a non-predictable manner. This might be due
268 to the spatial heterogeneity of the mechanical states within cells, as well as small
269 differences in optoLARG and rGBD expression levels in the stable cell lines. To address
270 this caveat, we reasoned that we should activate Rho using optoLARG with a more subtle
271 modality by illuminating only small ROIs and measuring small local fluctuations of Rho
272 activity using rGBD without inducing large changes in mechanical states. Further, to dissect
273 potential regulation of *DLC1* GAP activity by PI(4,5)P2 at the PM (Erlmann et al., 2009)
274 versus mechanosensitive interactions at the FA (Haining et al., 2018), we decided to make
275 measurements on FAs but use ROIs outside of FAs (non-FAs ROIs) to probe the PM. For
276 that purpose, we built an image analysis pipeline to first segment a cell in a field of view
277 and to then segment FAs based on their fluorescent intensity, size and localization at the
278 cell periphery using the paxillin-miRFP signal (Figure 5A). We then used these FA
279 segmentations to illuminate small ROIs within FAs or in neighboring non-FA ROIs with one
280 pulse of blue light using the DMD and evaluated rGBD fluorescence fluctuations at this
281 location for a couple of minutes until Rho activity returned to baseline (Figure 5B). This
282 optogenetic stimulation had no visible effect on edge retraction, or FA morphodynamics,
283 as observed when stimulating larger ROIs. Quality control of our automated segmentation
284 revealed high versus low paxillin signals in FA versus non-FA ROIs (Figure 5C). This
285 experiment was performed on multiple cells, allowing to average out any experimental
286 noise due to small differences in expression levels of optoLARG or rGBD. These data were
287 then averaged for FA and non-FA ROIs. We observed that this pulsed optoLARG light input
288 led to a local transient of Rho activity for approximately 2.5 minutes in WT cells when FAs
289 or the PM were stimulated (Figure 5D). The identical optoLARG input led to an increased
290 rate of Rho activation leading to higher amplitude when a FA versus a non-FA ROI was
291 stimulated. Surprisingly, in *DLC1* KO cells, we observed increased Rho activation rate that
292 also led to augmented Rho activity amplitude in comparison with WT cells in both FA and
293 non-FA ROIs. This was also accompanied with faster deactivation kinetics of RhoA. These
294 data suggest that DLC1 limits the rate of Rho activation rather than signal duration to
295 regulate RhoA activity in spread cells. This can occur both at the PM and at FAs. Further,
296 FAs seem to provide a subcellular environment that favors GEF-mediated activation of Rho
297 activity. The finding that *DLC1* KO also leads to faster deactivation suggests the existence
298 of a negative feedback that points to complex modalities of spatio-temporal regulation that
299 most likely involves additional GEFs/GAPs.

300

301 **DLC1 differently interact with FAs depending on their mechanical states**

302 Our finding that we did not observe striking patterns of RhoA activity in the vicinity of FAs
303 in spread cells challenges the idea that mechanical inputs regulate Rho activity in this
304 specific regime of mechanical forces. We speculated that the DLC1/talin system in FAs is
305 only mechanosensitive to stronger mechanical inputs. To evaluate FA-DLC1 interactions,
306 we imaged fibroblasts rescued with mCherry-DLC1 and miRFP-paxillin as a marker for
307 FAs. We observed that DLC1 binds to FAs at the onset of FA assembly, and that the local
308 DLC1 density augmented with the paxillin density (Figure S3A-C). During FA disassembly,
309 DLC1 density diminished concomitantly with decreasing paxillin density until the FA was
310 fully disassembled (Figure S3D-F).

311 To characterize force-dependent interactions of FAs with DLC1 in regimes of strong
312 mechanical perturbations, we engineered our mCherry-*DLC1* rescue cells to stably express
313 the optoLARG system, as well as the miRFP-paxillin construct. We then used the DMD to
314 activate Rho-mediated contractility locally and transiently in small ROIs containing FAs with
315 a standardized light input. The transient light pulse induced either of the two FA behaviors:
316 light-mediated FA reinforcement as evidenced by a local increase in paxillin density, was
317 followed by 1. FA relaxation (and decrease in paxillin density) upon light removal (Figure
318 6A-C, quantified in Figure 6D, Movie S5), or 2. FA rupture (Figure S4A-C). This was
319 accompanied by a striking simultaneous decrease in DLC1 intensity at the FA during FA
320 reinforcement, and a reassociation of DLC1 during FA relaxation upon light input removal.
321 If the light input led to FA rupture, then the DLC1 signal gradually decreased along FA
322 reinforcement until the FA ultimately ruptured in an all-or-nothing manner. FAs in the same
323 cell that were not subjected to the light input displayed dynamics as in normal cells, as
324 shown in Figure 6 (Figure S4D-F). These results indicate that DLC1 dynamically
325 dissociates and associates during acute FA reinforcement and relaxation in response to a
326 strong mechanical input.

327

328 Discussion

329 A key question in Rho GTPase biology is how multiple GEFs and GAPs control spatio-
330 temporal Rho GTPase signaling patterns to regulate cytoskeletal dynamics that power
331 morphogenetic processes such as cell migration. The recent finding that many GEFs and
332 GAPs themselves bind cytoskeletal and adhesion structures (Müller et al., 2020) strongly
333 suggests direct feedback from the cytoskeleton to Rho GTPase signaling. Self-
334 organizational properties of cytoskeletal and adhesions structures might therefore
335 contribute to spatio-temporal control of Rho GTPase signaling. Because DLC1 has been
336 proposed to bind to FAs in a mechanosensitive manner (Haining et al., 2018), we decided
337 to study it as a prototypical example of an adhesion feedback to Rho GTPase signaling.
338 Using novel technologies that allow for acute spatio-temporal perturbations, we provide

339 some new insights about how Rho GTPases are spatio-temporally controlled by a RhoGAP
340 that integrates mechanosensitive inputs.

341 We found that in spreading fibroblasts, *DLC1* KO globally augments contractility, as
342 illustrated by a robust increase in SFs and FAs (Figure 1). Evaluation of F-actin dynamics
343 immediately after spreading, when global contractility levels are still low, reveal that *DLC1*
344 KO fibroblasts rapidly assemble a wider contractile lamella than WT cells, suggesting
345 aberrant increase of myosin-based contractility already at an early stage of spreading
346 (Figure 2A). One hour after cell plating, when cells are well spread but still retain an
347 isotropic shape, we observed a global increase in contractility in *DLC1* KO versus WT cells
348 (Figure 3B). On a timescale of multiple hours after spreading, when WT cells break
349 symmetry, display polarized cell migration episodes, and finally adopt a contractile state
350 leading to a spindle morphology, we find that *DLC1* KO cells transition directly to the
351 contractile phenotype without being able to polarize (Figure 2C,D). Thus, DLC1 loss of
352 function leads to a global increase of aberrant contractility.

353 We had previously shown that REF52 fibroblasts display a wide band of RhoA activity that
354 correlates with the lamellar contractile myosin network during spreading (Martin et al.,
355 2016, 2014). We found that *DLC1* KO leads to a global increase in RhoA activity throughout
356 the cell, without however markedly modifying the spatial band of RhoA activity (Figure
357 3A,B). Similar results were observed when cells were allowed to further polarize and
358 assemble a robust actomyosin cytoskeleton (Figure 3C,D). Further, we observed that mild
359 DLC1 expression, that can still mostly be titrated by FAs and the PM without spilling out
360 into the cytosol, is already able to strongly downregulate global RhoA activity levels (Figure
361 S2B). We propose that DLC1 regulates global levels of RhoA activity at steady state, rather
362 than spatially patterned RhoA activity pools as observed in protrusive edges and filopodia
363 (Fritz et al., 2013; Machacek et al., 2009; Pertz et al., 2006), in the lamella (Martin et al.,
364 2016, 2014) or at the cytokinetic furrow (Basant and Glotzer, 2018; Bement et al., 2015b).
365 Note that the classic genetic perturbation paradigm cannot be used to study more subtle
366 functions of DLC1 at FAs because long-term loss of DLC1 function results in cells being
367 locked in a state of excessive contractility.

368 How does DLC1 contribute to the Rho GTPase flux in cells? To answer this question, we
369 used optoLARG to interrogate the Rho GTPase flux at the PM and at FAs, 2 sites at which
370 DLC1 can control Rho (Erlmann et al., 2009; Haining et al., 2018). We 1st found that a
371 transient optoLARG light input of identical amplitude at FAs led to increased Rho activity
372 amplitude compared to stimulation in non-FA PM regions (schematized in Figure 6E). This
373 strongly suggest that the FA is a subcellular region which is highly permissive for GEF-
374 mediated activation of Rho, which could involve a number of mechanisms including Src
375 regulation of Rho release from RhoGDI (DerMardirossian et al., 2006). 2nd, surprisingly,
376 we observed that *DLC1* KO cells displayed increased rates of Rho activation kinetics in
377 both FA and non-FA regions in response to a transient optoLARG light input, also leading

378 to increased Rho activity amplitude. This strongly suggests that DLC1 regulates the rate of
379 Rho activation rather than signal duration/termination. Given the promiscuous expression
380 of GEFs and GAPs within a cell type (Moon and Zheng, 2003; Rossman et al., 2005), other
381 Rho GAP(s) might specifically control signal termination, which might by example be
382 important to specifiy the lamellar pattern of RhoA activity in our REF52 cell system. The
383 role of DLC1 in controlling the rate of Rho activation remains to be understood. One can
384 however speculate that DLC1 provides negative feedback to control the rate of Rho
385 activation. Such feedback structures are prevalent in different GTPase signaling networks
386 (Tsyganov et al., 2012; Wu and Lew, 2013), and can endow the latter with properties such
387 as robustness to perturbations. 3rd, we observed that in addition to the increased rate of
388 Rho activation in response to the optoLARG input, *DLC1* KO cells also display faster
389 adaptation back to baseline Rho activity compared to control cells. Such non-linear
390 behavior again suggests the existence of additional feedback regulation that might involve
391 other GEFs/GAPs. An important feature of our optogenetic approach in which we perturb
392 cells minimally without eliciting cytoskeletal responses is that we might be able to capture
393 subtle dynamic processes occurring at steady state. Strong optoLARG input that leads to
394 robust actomyosin contractility and edge retraction, as seen in Figure 4, might activate
395 numerous mechanical feedback not present at steady-state, and thus not provide access
396 to cellular regulation processes occurring in an unperturbed, normal state.

397 Together, our data strongly suggests that in spread fibroblasts at steady state, in absence
398 of any acute mechanical input, DLC1 can exert its GAP activity both at the PM and at FAs
399 to control the rate of Rho activation. In these conditions, DLC1 association with FAs follows
400 FA assembly and disassembly (Figure 6), strongly suggesting that mechanosensitive
401 interactions with talin are not relevant in this context (Haining et al., 2018). Note that RhoA
402 localization is homogeneously distributed at the PM, and any RhoA pool being regulated
403 by DLC1 at the FAs will immediately diffuse in the PM, explaining the absence of local
404 pools of RhoA activity at FAs. This global regulation of RhoA activity levels by DLC1 in
405 fibroblasts is in marked contrast with neuronal growth cones, in which DLC1 regulates a
406 highly focused RhoA activity pattern that localizes to the tip of F-actin bundles in filopodia,
407 most probably to regulate formin-dependent actin polymerization (Fusco et al., 2016). In
408 this context, *DLC1* loss of function leads to an enlargement of the RhoA activity pattern at
409 filopodia, which results in longer and stabler filopodia, ultimately inducing more processive
410 growth cone motility and neurite outgrowth. This shows that a specific RhoGAP, such as
411 DLC1, can function in different ways in distinct cellular systems and mechanical contexts.

412 In the presence of acute mechanical perturbations, we observe distinct DLC1 dynamics at
413 FAs that most likely involve documented mechanosensitive interactions with talin at FAs
414 (Haining et al., 2018). Using optoLARG, we were able to control actomyosin contractility
415 transiently and locally in a small ROI leading to FA reinforcement followed by relaxation
416 (Figure 6). We found that in response to such a mechanical input, DLC1 rapidly dissociates

417 from FAs that exhibit robust reinforcement (Figure 6, schematized in Figure 6F). The
418 release of DLC1 in response to strong FA reinforcement correlates well with *in vitro*
419 measurements that have shown that DLC1 dissociates from stretched talin due to unfolding
420 of the r7-r8 domain (Haining et al., 2018). Our data also shows that FA relaxation can lead
421 to rebinding of DLC1 to FAs (Figure 6), suggesting that the r7-r8 talin domain might refold
422 in these conditions. Our results illustrate how optoLARG enables spatio-temporal,
423 reversible control of contractility that might help unravel mechanosensitive interactions that
424 are not accessible with classically used global chemical perturbations such as nocodazole-
425 mediated microtubule depolymerization (Krendel et al., 2002), or treatment with
426 lysophosphatidic acid (Pertz et al., 2006) leading to global RhoA activation and massive
427 stimulation of contractility.

428 We propose that DLC1 provides two levels of regulation of Rho. In absence of any strong
429 mechanical input, active DLC1 at FAs and at the PM throughout the cell seems to contribute
430 to the regulation of steady-state global Rho activity in the cells by controlling its rate of
431 activation. The significance of this mode of regulation is yet to be understood but most likely
432 involves simultaneous regulation with additional Rho GEFs and GAPs. Distinct Rho GAPs
433 might spatially control signal termination that shape the characteristic band of RhoA activity
434 that coincides with the lamella. In response to strong mechanical stimuli leading to FA
435 reinforcement and talin stretching, rapid unbinding of DLC1 from FAs might locally
436 decrease local RhoGAP activity providing positive feedback that could rapidly increase the
437 local rate of Rho activation, possibly strengthening contractility that might lead to FA
438 disassembly as we have observed. Conversely, when the mechanical input vanishes,
439 recruitment of DLC1 to relaxing FAs might rapidly switch off RhoA activity to return to a
440 steady state of low contractility. We speculate that these non-linear signaling behaviors
441 might allow to amplify local mechanical inputs to regulate all-or-nothing cytoskeletal
442 processes such as tail retraction during cell migration. Such tail retraction events are
443 characterized by short bursts of highly localized RhoA activity that are followed by rapid
444 relaxation once the tail has been retracted (Martin et al., 2014; Pertz et al., 2006). Here,
445 SF pulling on FAs at the back of a cell might allow local release of DLC1, rapid increase of
446 local RhoA activity, leading to strong local contraction and tail retraction. Experimentally
447 testing this hypothesis in the context of tail retraction is technically challenging because
448 long term DLC1 perturbation leads to global contractility that precludes cell polarization,
449 directional migration and thus tail retraction episodes. This illustrates an important limitation
450 of the classic genetic perturbation toolkit that has been used to study Rho GTPase
451 signaling.

452 Our results provide new insights into the complex network circuitry that regulates spatio-
453 temporal Rho GTPase signaling and illustrate how we must tackle this problem. By allowing
454 for precise and reversible perturbations, signaling optogenetics provide the opportunity to
455 dissect the spatio-temporal Rho GTPase fluxes that control patterns of Rho GTPase

activity at adequate time/length scales. In the future, a full understanding of Rho GTPase signaling fluxes and formation of signaling patterns will require more systematic approaches to consider the multiple GEFs/GAPs that are involved in shaping cell morphogenesis.

Materials and methods

Cell culture

Rat Embryo Fibroblast 52 (REF52) were cultured in Dubelcco's Modified Eagle Medium with 4.5 g/l glucose, 10% 4mM L-Glutamine, and 100 U/ml penicillin/streptomycin. Cells were grown at 37 ºC and 5% CO2.

SiRNA knockdown

4µl lipofectamine RNAi max was mixed with a total of 500µl of OPTIMEM medium and a pool of SiRNAs against the gene of interest at a final concentration of 60 nM (SiTools Biotech). The mix was added to a 6 well plate containing 100000 cells in a 2 ml medium volume medium.

CrispR/Cas9 Knockout generation

Two guide sequences targeting DNA within exon 5 of the DLC1 gene were selected using the CRISPOR tool for predicted high-specificity protospacer adjacent motif target sites in the rat genome [32] . Two complementary oligos each containing the DLC1 guide sequence and Bbsl ligation adapters were synthesized (Microsynth) (sense sequence: 5'-CACCGAACCGAGAGAGCTACCCGG-3', antisense sequence: 5'-AAACCCGGGTAGCTCTCTCGGTTC-3'). The guide sequences were annealed and ligated into a pSpCas9(BB)-2A-GFP vector. REF52 cells were grown in six-well plates to 60% confluency and transfected with 1µg of the vector together with 1 µl of Lipofectamine 3000 and 5 µl of P3000 solution (ThermoFisher Scientific). Two days post transfection cells were detached, suspended in PBS +1% FBS and sorted into 96 well-plates using fluorescence-activated cell sorting. After expansion, individual clones were detached and suspended in the lysis buffer (10mM TRIS, 50mM KCL, 2.5mM MgCl2, 0.45% Tween-20, 0.05% Gelatine, 0.12 mg/ml of proteinase K). The cell solution was frozen at -80 °C and subsequently kept at 63 °C for one hour. Proteinase K was inactivated by heating the solution to 95 °C for 15 minutes. PCR primers were designed to amplify a 500bp region around the CRISPR cut site (forward primer: 5'-AAGGAGTGTGTCTAACTCCACGCAGACCAG-3', reverse primer: 5'-

491 CTCCTTAGGACTGTCGCTGCTGTTTTCTCT-3'). Genomic sequences were amplified by
492 PCR and sequenced by Sanger sequencing.

493

494 **DNA constructs**

495 A "pB3.0" piggybac vector was created by adapting the pPBbsr2 (Matasci et al., 2011) to
496 make it smaller in size. pPBbsr2 was digested with AscI and PacI, yielding 3922 bp and
497 2864 bp fragments. Full size pPBbsr2 was used as template for a PCR with forward primer
498 5'-TTAGCATTAATTAAGCGGCCGCGTTGCTGGCGTTTTTCC-3' and reverse primer 5'-
499 GTGCCTTTACAACTTATGAGTAACCCCGCGCGGACGATT-3', yielding a 1671bp insert
500 that was ligated back into the receiving 3922bp part of the digested pPBbsr2 vector,
501 creating "pB3.0-BLAST" (Blasticidine resistance). To introduce different resistance
502 cassettes, we performed an overlap extension PCR with pB3.0-BLAST as template for
503 PCR1 (primers A+B) and PCR2 (primers C+D) with the following primers:

504 primer A: 5'-AAGGATGCCCAGAAGGTACCCCATTGTATGGGATCTGATCTGGG-3',
505 primer B: 5'-GGAAACTTTTTGTGCTATTATGGTGGCCATTCAGCTCTACGTAGCTACT-
506 3', primer C 5'-
507 CCTTTGAAAAACACGATAATACCACCGGTAAGTCGAGATGCATCGATGA-3', primer D:
508 5'-CTCCGCCTTTCTTGGACGTCGGGTTCGAACCGCATTAGT-3'. Primers A and D, the
509 product of PCR1 and PCR2 were used for fusing the two fragments by PCR. The resulting
510 PCR product was ligated into the pB3.0-BLAST vector, digested with Kpn1 and Pst1, by
511 fusion cloning, yielding a pB3.0-noAB vector with a single Age1 site to introduce antibiotic
512 resistance cassettes. To produce pB3.0-HYGRO and pB3.0-PURO, PCRs were performed
513 on template vectors pHygro-PB and pPuro-PB, respectively. For pB3.0-HYGRO forward
514 primer 5'-AACACGATAATACCACCATGAAAAAGCCTGAACTCACCGC-3' and reverse
515 primer
516 5'-GCAGGCTCCCGTTTCCTTATCGGCCATTCAGCTCTA-3' were used. For pB3.0-
517 PURO forward primer 5'-AACACGATAATACCACCATGACCGAGTACAAGCCCACG-3'
518 and reverse primer 5'-GCGTTCGGGCCACGGACTGGCCATTCAGCTCTA-3' were used.
519 The respective inserts were inserted via fusion cloning in the pB3.0-noAB vector [33],
520 digested with AgeI.

521 Construction of the pB3.0-optoLARG-mVenus-SspB-p2A-stargazin-mtq2-iLID optoLARG
522 system was as follows. The cDNA for optoLARG-mVenus-SspB(nano)-p2A-iLID-CAAX
523 was synthesized by custom gene synthesis (Genewiz, Azenta life sciences, US). The
524 sequence contained the catalytical DH-PH domain of human RhoGEF12 (LARG, aa 766-
525 1138), connected via a linker (GSGSGSGS) to full-length mVenus fused to SSPB(nano).
526 This is followed by a p2A sequence (GSGATNFSLLKQAGDVEENPGP), the iLID module
527 (Guntas et al., 2015) and a CAAX box (KRAS). The construct was cloned into pB3.0-BLAST
528 containing a CAG promotor, yielding pB3.0-optoLARG-mVenus-SspB-p2A-iLID-CAAX.

529 After publication of an improved plasma membrane anchor for the iLID-module (Natwick
530 and Collins, 2021), we changed the part after the p2A sequence. The pB3.0-optoLARG-
531 mVenus-SspB-p2A-iLID-CAAX vector was digested with BsrGI and AflII, and a custom
532 gene synthesized stretch of cDNA containing SspB(nano)-p2A, full-length stargazin,
533 mTurqoise2 and iLID was inserted. This yielded pB3.0-optoLARG-mVenus-SspB(nano)-
534 p2A-stargazin-mtq2-iLID (exact sequences of the gene synthesis products are available on
535 request).

536 An eGFP DLC1 plasmid containing the 1091aa long isoform originating from mouse (kindly
537 provided by Monilola A. Olayioye) was used to produce mCherry-DLC1. The DLC1 gene
538 was cut out of this plasmid with BamHI and, N-terminally fused to FKBP12-mCherry and
539 inserted into pB3.0-BLAST containing a CAG-promotor, yielding pB3.0-FKBP12-mCherry-
540 DLC1.

541

542 **Spreading Assay**

543 Glass bottom well plates (Celvis) were coated with 5 µg/ml of human plasma fibronectin
544 purified protein (Merck) for one hour at room temperature. REF52 cells were seeded at a
545 density of 7000 cells per well (using 24 well plates) in FluoroBrite DMEM medium
546 containing 1% FBS, 0.1% BSA, 4mM L-Glutamine and 100 U/ml penicillin/streptomycin.
547 Imaging was done with a Nikon Eclipse Ti-E inverted microscope with an automatic stage.
548 Temperature was kept at 37ºC with a temperature control system, humidity (100%) and
549 CO2 (~5%) with a gas mixer (Life Imaging Services). Focus drift was prevented by the
550 equipped Perfect Focus System (Nikon). The microscope was controlled with Metamorph
551 software (Universal Imaging).

552

553 **Optogenetic Stimulation experiments**

554 Glass bottom well plates (Celvis) were coated with 5 µg/ml of human plasma fibronectin
555 purified protein (Merck) for one hour at room temperature. REF52 cells were seeded at
556 6000 cells/well into 12 well plates and allowed to attach for 12 hours. For both RhoA activity
557 and mCherry-DLC1/miRFP-paxillin optogenetic stimulation experiments cells were
558 incubated in FluoroBrite DMEM medium overnight. The microscope was controlled with
559 NIS-Elements (Nikon) for observing DLC1 dynamics and with open-source micromanager
560 software (Edelstein et al., 2014) for edge stimulation. Optogenetic stimulation was localized
561 to specific regions using an Andor mosaic 3 DMD. For mCherry-DLC1/miRFP-paxillin
562 experiments, ROIs were user-defined. For RhoA activity experiments, cells in different
563 fields of view were selected by a user, cells were then segmented with a custom pixel-
564 classifier based on a pre-trained VGG16 convolutional neural network, which was trained

565 on a field of view of the experimental data. ROIs for stimulation masks were then
566 automatically defined at the top and bottom of the cell for consecutive illumination with
567 different light pulse regimes. Fields of views were imaged one after the other on multiple
568 cells. For data extraction the stimulation mask was expanded by gaussian smoothing and
569 then thresholded to cover a wider region, reducing artifacts caused by membrane
570 dynamics. Image intensities were calculated for the overlap of this mask with the
571 segmented cells and the full segmented cells respectively.

572

573 **Immuno-histochemistry**

574 One hour after seeding, cells were fixed for 10 minutes with 0.2% paraformaldehyde. A
575 0.1% Triton X solution was used for permeabilization, after which cells were incubated
576 overnight at 4C with the blocking buffer, containing 5% Bovine-Serum-Albumin and 0.05%
577 Tween20 in PBS. After each step of the following protocol cells were washed three times
578 with Phosphate-Buffered-Saline (PBS). Cells were incubated overnight with the primary
579 antibody (1:250 dilution for paxillin (Abcam ab32084), 1:50 for pMLC (Cell Signaling
580 Antibody #3671). Secondary antibody incubation (1:1000) lasted one hour. Phalloidin
581 incubation (1:200 Phalloidin-Atto647N) was performed for 20 minutes and DAPI incubation
582 for 10 hours. Cells were imaged immediately after the last step.

583

584 **Image analysis**

585 Lamella size, focal adhesion areas (Figure 1) and RhoA activity ratio measurements
586 (Figure 3) were computed with CellProfiler in conjunction with a pixel classifier trained with
587 Ilastik (Berg et al., 2019). Spreading dynamics (Figure 2D) were manually analyzed. FRET
588 ratio images were computed and analyzed with custom python scripts. DLC1 and paxillin
589 dynamics (Figure S3D) were calculated with manually drawn ROIs in Fiji (Schindelin et al.,
590 2012).

591

592 Acknowledgements

593 This work was supported by the Swiss National Science Foundation IZSAZ3_173462
594 Argentinian-Swiss Joint Research Programme and by the Sinergia CRSII5_183550 grants
595 to Olivier Pertz. We are grateful to the Microscopy Imaging Center of the University of Bern
596 for support (https://www.mic.unibe.ch). We thank Kazuhiro Aoki (NIBB, Japan) for providing
597 the pPBbsr2 vector, David L. Hacker (EPFL, Switzerland), for the pPuro-PB and pHygro-
598 PB plasmids, Judith Trüb (UniBE, Switzerland) for the cloning of pB3.0-BLAST, Monilola
599 A. Olayioye (University of Stuttgart, Germany) for the eGFP DLC1 plasmid, Dean E.

Natwick and Sean R. Collins (University of California Davis) for sharing the Stargazin-iLID constructs. We are grateful to Miguel Vicente-Manzanares, Bernhard Wehrle-Haller and Daniel Riveline for constructive comments on the manuscript

Author contributions

O.P. supervised the research. O.P. and M.H. wrote the paper. M.H. designed and performed experiments. L.H. designed and performed optogenetic experiments. J.v.U. built the optoLARG/rGBD circuit. M.D. designed data analysis tools.

Additional Information

The authors declare no competing interests.

Figure legends.

Figure 1. Cytoskeletal structures in WT and DLC1 deficient cells.

A,B. Representative immunofluorescence images of paxillin and F-actin (phalloidin) (**A**), and pMLC and F-actin (phalloidin) (**B**) immunostains are shown in inverted black and white (ibw) contrast as well as color composites (DAPI signal also included). Scale bar = 10µm.

C. Compared to WT cells (n=243) lamella size is significantly increased in *DLC1* KD cells (n=290, p-adjusted < 0.001) and *DLC1* KO cells (n=242, p-adjusted < 0.001), while *DLC1* rescue cells (n=57) show significantly lower lamella sizes than both, WT (p-adjusted = 0.0098), as well as KO cells (p-adjusted < 0.001).

D. *DLC1* KD cells (n=290) display a significant increase in the total area of focal adhesions per cell (p-adjusted <0.001) compared to WT cells (n=243), while DLC1 KO cells (n=242) do not show a significant difference (p-adjusted = 0.09). Rescue cells show a significant decrease in the total area of focal adhesions (p-adjusted < 0.001). ANOVA plus Tukey's honestly significant difference test.

Figure 2. F-actin dynamics and cell morphodynamics in WT and DLC1 KO cells.

All time series are representative ibw contrast images of WT and *DLC1* KO cells expressing Lifeact-mCherry. Dotted lines mark the area used for the kymographs shown in the right panels.

A. Cells were imaged for 10 minutes in 10 second intervals during spreading immediately after replating. Dotted red lines display differences in lamella size in WT and *DLC1* KO cells. Time

B. One hour after reseeding, when cells are still isotropically spreading, *DLC1* KO cells display increased lamellipodia size and more prominent edge protrusion retraction cycles. High magnification insets are shown for time point 10 minutes and show the robust increase of contractility in *DLC1* KO cells.

C. Cells were imaged for 10 hours with 15 minutes intervals starting from spreading. WT cells break symmetry and display episodes of polarized motility. KO cells are much less dynamic and reach a contractile phenotype much faster, without being able to polarize.

D. Box plot showing at which time point cells exhibited the elongated phenotype described in (**C**). *DLC1* KO cells (n=42) exhibited this phenotype a mean of 90 minutes earlier than WT cells (n=22) p-adjusted = 0.002, Student's t-test. 17 additional WT cells failed to develop that phenotype entirely.

646 Scale bars = 20 μm for all images.

647

648 **Figure 3. RhoA activation dynamics in WT and DLC1 KO cells**

649 Cells are stably expressing Lifeact-mCherry, and the RhoA2G FRET sensor. RhoA
650 localization images show RhoA2G localization that is identical to RhoA. RhoA activity
651 images display the computed FRET ratio. Images are color-coded according to the
652 normalized scales shown below the panels.

653 **A**. Representative images of WT and *DLC1* KO cells during spreading. Kymographs for the
654 violet lines are shown in the right panels. Note the RhoA activity band maintains constant
655 width during spreading at the periphery in WT cells. Note increased global RhoA activity in
656 *DLC1* KO cells, with maintenance of a similar RhoA band pattern at the cell edge.

657 **B.** Box plots of FRET ratio averaged over the whole cell (right panel) or a ROI placed at
658 the cell edge (left panel). This shows that during spreading *DLC1* KO cells (n = 149) have
659 an increased total RhoA activity compared to WT cells (n = 114, p = 0.005). In addition, the
660 FRET ratio at just the cell edge is increased as well (p=0.011).

661 **C.** Representative images of WT cells and DLC1 KO cells that have transitioned in a
662 contractile state 12 hours after plating. No difference in RhoA activity pattern can be
663 observed between WT and *DLC1* KO cells, although the latter still display slightly higher
664 global RhoA activity levels.

665 **D.** Box plots of FRET ratio averaged over the whole cell (right panel) or a ROI placed at
666 the cell edge (left panel). This shows that contractile *DLC1* KO cells (n=103) have an
667 increased total RhoA activity (p < 0.001) and edge FRET ratio (p < 0.001) compared to WT
668 cells (n = 82) compared to WT cells (n = 82). Students t-test.

669 (A,B) Scale bars = 20 μm.

670

671 **Figure 4. An optogenetic actuator- Rho biosensor circuit to probe Rho**
672 **GTPase flux**

673 **A.** Schematics of the optogenetic actuator - Rho biosensor to measure Rho GTPase flux.
674 OptoLarg is based on an iLID system which does not interact with Ssb-LARG in the dark
675 state. The iLID module is anchored to the plasma membrane by a Stargazin anchor that
676 displays slow diffusion, allowing better focussing of optogenetic activation. Upon light
677 exposure ssb-LARG is locally recruited to the plasma membrane, activating Rho. Rho
678 activity is measured by a rGBD effector binding domain.

679 **B.** Time-series of REF52 cells locally stimulated with light first in a ROI at the cell top with
680 a high stimulation frequency, and then with a ROI at the cell bottom with a low stimulation
681 frequency. Light pulses have the same intensity. Thick and thin blue thunder symbols
682 represent high and low optogenetic stimulation. Red dotted line is used for the kymograph
683 shown in (C).

684 **C.** Kymographs of cells in (B). Light pulse stimulation regimes of top and bottom ROIs are
685 shown in the upper box. Blue dotted boxes indicate the region and length of the stimulation.

686 Note how intense optogenetic stimulation in the top ROI leads to Rho activity, assembly of
687 contractile F-actin structures, and robust edge retraction. Upon removal of the light input,
688 the Rho activity and F-actin resume, and edge protrusion occurs again. Lower optogenetic
689 stimulation in the bottom ROI leads to much lower Rho activity and F-actin structures, as
690 well as lower edge retraction.

691 (**B**,**C**) Scale bars = 10 μm

692

693 **Figure 5. Rho GTPase activation kinetics in WT versus DLC1 KO cells**

694 **A**. Computer vision pipeline and experiment: 1) a cell is segmented using the rGBD-dTomato
695 channel. 2) FAs and non-FAs are detected using the paxillin channel (see Material and
696 Methods). ROIs on FAs (blue dots, shown in the bottom left panel) and ROIs on non-FA
697 regions in between (orange dots, shown in the upper left panel) are selected for stimulation.
698 3) Image of the stimulation pattern (green channel) shows that the calibrated DMD can
699 stimulate the regions with high spatial precision (image is overexposed to show the
700 diffraction pattern of the mirrors).

701 **B**. The DMD is used to stimulate ROIs (FAs or non-FAs) with a pulse of blue light (blue line).
702 rGBD signal fluctuations are then measured in the ROIs.

703 **C**. Distribution of paxillin-miRFP intensities in the FA and Non-FA ROIs normalized to the
704 mean paxillin-miRFP intensity of the whole cell shows that our segmentation pipelines
705 accurately identifies FA and Non-FA ROIs.

706 **D.** Normalized and averaged rGBD fluorescence fluctuations upon ROI optogenetic
707 stimulation. For each stimulated ROIs, the fold change to the baseline (average activity from
708 0-150 seconds before optogenetic stimulation) is calculated. Median and 99% CI are shown.
709 Regions on top of focal adhesions have a larger fold change in rGBD activity than regions
710 between focal adhesions. DLC1-KO cells have a larger rGBD fold change in the initial time
711 after stimulation (150-200 seconds), but then also fall back down to the baseline quicker.
712 (KO-FA: N=3643, KO-NON-FA: N=3643, CTRL-FA: N = 2144, CTRL-NON-FA:2144. Mean
713 number of regions per cell: ~16.90, Cells CTRL = 321, DLC1-KO=431. The same cell can

714 appear multiple times in the experiment, but with a relaxation time in between and new
715 stimulation regions).

716 **E.** The different dynamics described in (**D**) can be robustly observed in technical replicates
717 of the experiment. In all replicates the rGBD recruitment is higher in FAs vs Non-FAs, and
718 we see the trend of faster accumulation and faster return to baseline of rGBD in DLC1 KO
719 vs CTRL cells.

720

721 **Figure 6. Optogenetic control of force-dependent DLC1 interactions with FAs**

722 **A.** Color-coded fluorescence micrographs of REF52 fibroblast expressing miRFP-paxillin
723 (left) and mCherry-DLC1 (right) and the optoLARG construct (not shown). The black boxes
724 indicate the area used for close up images in (B). The white boxes indicate the ROI for
725 optogenetic illumination. Selected FAs denoted by the pink and green arrowheads. The
726 black dotted lines were used for the kymograph in B.

727 **B.** Kymographs showing two selected FAs, the grey box indicates the time at which
728 optogenetic stimulation has been applied. Optogenetic stimulation is applied on select
729 ROIs placed over FAs with 50 ms light pulses per frame (every 15 seconds) for a duration
730 of 7.5 minutes.

731 **C.** Closeups time series of paxillin and DLC1 signals at a single FA denoted by the
732 respective arrowheads. Scale bars = 10 µm.

733 **D.** Quantification of mcherry-DLC1 and miRFP-paxillin fluorescence signals during
734 optoLARG mediated control of FA reinforcement and relaxation. Normalized miRFP-
735 paxilllin and mCherry-DLC1 from 2 FAs shown in panels A-C.

736 **E.** Model of Rho GTPase activity modulation by DLC1 at FAs and at the plasma membrane
737 relevant to Figure 5. Left and right panels show schematics of Rho activation dynamics in
738 response to optoLARG optogenetic input at FAs (left panel) and plasma membrane (right
739 panels). Top and bottom panel show schematics for Rho activation dynamics in response
740 to optoLARG optogenetic input in control (top) and DLC1 KO (bottom) panels.

741 **F.** Model of force dependent regulation of DLC1 at FAs relevant to this and Figure S3. Left
742 panel, in absence of acute mechanical input, DLC1 increases with FA assembly and
743 decreases with FA disassembly. Central panel, upon acute local increase of mechanical
744 stress in response to application of an optoLARG optogenetic input, DLC1 unbinds from
745 FA in a reinforcement regime, and rebinds FA in a relaxing regime when the optoLARG
746 input is removed. Right panel, upon acute local increase of mechanical stress in response
747 to application of an optoLARG optogenetic input some FAs rupture after DLC1 dissociation
748 and FA rupture.

Supplementary Figure legends

Figure S1: Cell motility properties in WT versus DLC1 KO cells

A. Example fields of view of tracked WT and *DLC1* KO cells. 20000 REF fibroblasts expressing a histone H2B-miRFP marker were seeded in a 24 well-plate well coated with fibronectin and stimulated with 20 ng/ml PDGF, imaged for 12 hours at 15 minutes interval. Tracking was performed using stardist [37] on the H2B image). *DLC1* KO cells display a large subpopulation of cells that remain extremely stationary.

B. Mean Square displacements (MSDs) for different time intervals, WT move more than *DLC1* KO cells for all possible lag times. Plot shows directionality (exponential bit between 0.25 and 1.5 hours). For times longer than 2 hours the curve is flat indicating that migration has characteristics of random walk at these timescales. Thick lines: mean, thin lines: standard deviation. Dotted grey line shows delta t chosen for figure C.

C. Distribution of velocities calculated as µm/hour from Root-MSD. We again observe the bimodal distribution in the *DLC1* KO cell with a big subgroup of the cells move extremely slowly (5 µm/hour). Thick lines are mean and extrema. Two sided t-test: (statistic=25.1, p-value=1.6e-131)

Figure S2. Effect of DLC1 overexpression on F-actin cytoskeleton and RhoA activity

A. Effect of DLC1 overexpression of F-actin. REF52 cells stably expressing Lifeact-mCherry were transfected with mCherry-DLC1 or mCherry plasmids, allowed to spread for 12 hours on fibronectin-coated coverslips and imaged. Images are shown in ibw contrast. Large mCherry-DLC1 pool in the cytosol levels documents its overexpression. Note how DLC1 overexpression leads to loss of contractile F-actin structures.

B. Effect of DLC1 overexpression of RhoA. Cells stably transfected with the RhoA2G biosensor were transfected with mCherry-paxillin or mCherry-DLC1. mCherry signals are shown in ibw contrast. RhoA2G FRET ratio, and expression levels are color-coded according to the scale. Note how low mCherry-DLC1 expression that remains associated with FA already lowers RhoA activity, while high mCherry-DLC1 expression leads to even lower RhoA activity and aberrant cell morphology.

Figure S3. DLC1 dynamics at FAs in unperturbed cells

Panels **A-C** document FAs in an assembly state. This shows that the DLC1 signal augments concomitantly with paxillin signal during FA assembly.

783 Panels **D-F** document FAs in a disassembly state. This shows that the DLC1 signal
784 decreases concomitantly with paxillin signal during FA disassembly.

785 **A,D.** Color-coded fluorescence micrographs of REF52 fibroblast expressing miRFP-paxillin
786 (top) and mCherry-DLC1 (bottom). The white boxes indicate the area used for close up
787 images in (B,E).

788 **B,E.** Closeups of the ROIs (left panel) and kymographs (right panel) of selected FAs
789 denoted by the red arrowheads. White dotted lines were used for the kymograph. In the
790 kymograph, the grey box indicates the time at which optogenetic stimulation has been
791 applied.

792 **C,F.** Closeups time series of paxillin and DLC1 signals at a single FA denoted by the
793 respective red arrowheads.

794 Scale bars = 10 μm.

795

796 **Figure S4. DLC1 dynamics in an optoLARG stimulated FA that undergoes**
797 **reinforcement followed by disassembly, as well as FA behavior in absence**
798 **of optoLARG stimulus**

799 Panels **A-C** document FAs that when subjected to a nearby pulse of optogenetic Rho-
800 mediated contractility display a behavior of FA reinforcement followed by disassembly.
801 Optogenetic stimulation is applied on select ROIs placed over FAs with 50 ms light pulses
802 per frame (every 15 seconds) for a duration of 8 minutes.

803 Panels **D-F** document the dynamics of DLC1 in a ROI not stimulated with light in the same
804 cell as in shown in Figure 6A-C.

805 **A.** Color-coded fluorescence micrographs of REF52 fibroblast expressing miRFP-paxillin
806 (top) and mCherry-DLC1 (bottom) and the optoLARG construct (not shown). The black
807 boxes indicate the area used for close up images in (B). The white boxes indicate the ROI
808 for optogenetic illumination.

809 **B.** Closeups of the ROIs (left panel) and kymographs (right panel) of selected FAs denoted
810 by the arrowheads. The pink and green arrowheads indicate the FAs of interest in (B). The
811 black arrowhead indicates the FA of interest in (C). The black dotted lines were used for
812 the kymograph. In the kymograph, the grey box indicates the time at which optogenetic
813 stimulation has been applied.

814 **C.** Closeups time series of paxillin and DLC1 signals at a single FA denoted by the
815 respective arrowheads. Scale bars = 10 μm.

D. Color-coded fluorescence micrographs of REF52 fibroblast expressing miRFP-paxillin (top) and mCherry-DLC1 (bottom) and the optoLARG construct (not shown). The black boxes indicate the area used for close up images in (B,E). The white boxes indicate the ROI for optogenetic illumination.

E. Closeups of the ROIs (left panel) and kymographs (right panel) of selected FAs denoted by the arrowheads. The pink and green arrowheads indicate the FAs of interest in (B). The black arrowhead indicates the FA of interest in (D). The black dotted lines were used for the kymograph. In the kymograph, the grey box indicates the time at which optogenetic stimulation has been applied.

F. Closeups time series of paxillin and DLC1 signals at a single FA denoted by the respective arrowheads.

Supplementary Movie legends

Movie S1: F-actin dynamics of WT and DLC1 KO REF52 cells during late spreading (relevant to Figure 2B).

Representative ibw contrast movie of WT and *DLC1* KO cells expressing Lifeact-mCherry during late spreading. Time: Minutes:seconds. Scale bar = 20 mm.

Movie S2: F-actin dynamics and edge dynamics of WT and DLC1 KO REF52 cells during acquisition of a polarized cell migration phenotype over a period of 15 hours (relevant to Figure 2C).

Representative ibw contrast movie of WT and *DLC1* KO cells expressing Lifeact-mCherry for 15. Edge dynamics were color-coded with respect to time. Time: Minutes:seconds. Scale bar = 20 mm.

Movie S3: F-actin and RhoA activity dynamics WT and DLC1 KO REF52 cells during late spreading (relevant to Figure 3A).

Representative movie of WT and *DLC1* KO cells expressing Lifeact-mCherry and the RhoA2G FRET biosensor during late spreading.

Left panels: F-actin channel in ibw contrast. Right panels: RhoA activity emission ratio color coded according to color scale.

848 Time: Minutes:seconds. Scale bar = 20 mm.

849

850 **Movie S4: Characterisation of the optoLARG/rGBD genetic circuit (relati to**
851 **Figure 5)**

852 REF52 cells stably expressing the optoLARG/rGBD circuit as well as Lifeact-miRFP are
853 locally stimulated with blue light of identical intensity, first in a ROI at the cell top with a high
854 stimulation frequency, and then with a ROI at the cell bottom with a lower stimulation
855 frequency. The stimulation frequencies are indicated by the appearance/disappearance
856 frequency of the ROIs.

857 Left panel: rGBD signal, Right panel: F-actin lifeact-miRFP. Note the more robust edge
858 contraction, as well as increased RhoA activity in response to high versus low light
859 frequency stimulation.

860 Time: Minutes:seconds. Scale bar = 10 mm.

861

862 **Movie S5: DLC1 dynamics at FAs during an optoLARG-induced contractility**
863 **pulse (relevant to Figure 6A-C, cell denoted by pink arrow)**

864 REF52 KO cells rescued with mCherry-DLC1 and expressing miRFP-paxillin, and the
865 optoLARG/rGBD circuit were imaged before, during and after a transient optogenetic
866 stimulation in the whole field of view shown in the movie.

867 Time: Minutes:seconds. Scale bar = 5 mm.

References

Basant A, Glotzer M. 2018. Spatiotemporal Regulation of RhoA during Cytokinesis. *Curr Biol* **28**:R570–R580.

Bement WM, Leda M, Moe AM, Kita AM, Larson ME, Golding AE, Pfeuti C, Su K-C, Miller AL, Goryachev AB, von Dassow G. 2015a. Activator-inhibitor coupling between Rho signalling and actin assembly makes the cell cortex an excitable medium. *Nat Cell Biol* **17**:1471–1483.

Bement WM, Leda M, Moe AM, Kita AM, Larson ME, Golding AE, Pfeuti C, Su K-C, Miller AL, Goryachev AB, von Dassow G. 2015b. Activator–inhibitor coupling between Rho signalling and actin assembly makes the cell cortex an excitable medium. *Nat Cell Biol* **17**:1471–1483.

Bement WM, von Dassow G. 2014. Single cell pattern formation and transient cytoskeletal arrays. *Curr Opin Cell Biol* **26**:51–59.

Berg S, Kutra D, Kroeger T, Straehle CN, Kausler BX, Haubold C, Schiegg M, Ales J, Beier T, Rudy M, Eren K, Cervantes JI, Xu B, Beuttenmueller F, Wolny A, Zhang C, Koethe U, Hamprecht FA, Kreshuk A. 2019. ilastik: interactive machine learning for (bio) image analysis. *Nat Methods* **16**:1–7.

Blum Y, Mikelson J, Dobrzyński M, Ryu H, Jacques M-A, Jeon NL, Khammash M, Pertz O. 2019. Temporal perturbation of ERK dynamics reveals network architecture of FGF2/MAPK signaling. *Mol Syst Biol* **15**:e8947. doi:10.15252/msb.20198947

DerMardirossian C, Rocklin G, Seo J-Y, Bokoch GM. 2006. Phosphorylation of RhoGDI by Src regulates Rho GTPase binding and cytosol-membrane cycling. *Mol Biol Cell* **17**:4760–4768. doi:10.1091/mbc.e06-06-0533

Dessauges C, Mikelson J, Dobrzyński M, Jacques M, Frismantiene A, Gagliardi PA, Khammash M, Pertz O. 2022. Optogenetic actuator – ERK biosensor circuits identify MAPK network nodes that shape ERK dynamics. *Mol Syst Biol* **18**. doi:10.15252/msb.202110670

Edelstein AD, Tsuchida MA, Amodaj N, Pinkard H, Vale RD, Stuurman N. 2014. Advanced methods of microscope control using μManager software. *J Biol Methods* **1**. doi:10.14440/jbm.2014.36

Erlmann P, Schmid S, Horenkamp FA, Geyer M, Pomorski TG, Olayioye MA. 2009. DLC1 activation requires lipid interaction through a polybasic region preceding the RhoGAP domain. *Mol Biol Cell* **20**:4400–4411. doi:10.1091/mbc.e09-03-0247

Etienne-Manneville S, Hall A. 2002. Rho GTPases in cell biology. *Nature* **420**:629–635.

Fritz RD, Letzelter M, Reimann A, Martin K, Fusco L, Ritsma L, Ponsioen B, Fluri E, Schulte-Merker S, van Rheenen J, Pertz O. 2013. A versatile toolkit to produce sensitive FRET biosensors to visualize signaling in time and space. *Sci Signal* **6**:rs12. doi:10.1126/scisignal.2004135

Fritz RD, Pertz O. 2016. The dynamics of spatio-temporal Rho GTPase signaling: formation of signaling patterns. *F1000Research* **5**. doi:10.12688/f1000research.7370.1

Fusco L, Lefort R, Smith K, Benmansour F, Gonzalez G, Barillari C, Rinn B, Fleuret F, Fua P, Pertz O. 2016. Computer vision profiling of neurite outgrowth dynamics reveals

spatiotemporal modularity of Rho GTPase signaling. *J Cell Biol* **212**:91–111. doi:10.1083/jcb.201506018

Gingras AR, Bate N, Goult BT, Hazelwood L, Canestrelli I, Grossmann JG, Liu H, Putz NSM, Roberts GCK, Volkmann N, Hanein D, Barsukov IL, Critchley DR. 2008. The structure of the C-terminal actin-binding domain of talin. *EMBO J* **27**:458–469. doi:10.1038/sj.emboj.7601965

Goult BT, Brown NH, Schwartz MA. 2021. Talin in mechanotransduction and mechanomemory at a glance. *J Cell Sci* **134**:jcs258749. doi:10.1242/jcs.258749

Graessl M, Koch J, Calderon A, Kamps D, Banerjee S, Mazel T, Schulze N, Jungkurth JK, Patwardhan R, Solouk D, Hampe N, Hoffmann B, Dehmelt L, Nalbant P. 2017. An excitable Rho GTPase signaling network generates dynamic subcellular contraction patterns. *J Cell Biol* **17**:jcb.201706052-15.

Guntas G, Hallett RA, Zimmerman SP, Williams T, Yumerefendi H, Bear JE, Kuhlman B. 2015. Engineering an improved light-induced dimer (iLID) for controlling the localization and activity of signaling proteins. *Proc Natl Acad Sci U S A* **112**:112–117.

Haining AWM, Rahikainen R, Cortes E, Lachowski D, Rice A, von Essen M, Hytönen VP, del Río Hernández A. 2018. Mechanotransduction in talin through the interaction of the R8 domain with DLC1. *PLOS Biol* **16**:e2005599-20.

Hu J, Gong X, Strömblad S. 2022. Local temporal Rac1-GTP nadirs and peaks restrict cell protrusions and retractions. *Sci Adv* **8**:eabl3667. doi:10.1126/sciadv.abl3667

Isogai T, Danuser G. 2018. Discovery of functional interactions among actin regulators by analysis of image fluctuations in an unperturbed motile cell system. *Philos Trans R Soc B Biol Sci* **373**:20170110. doi:10.1098/rstb.2017.0110

Itoh RE, Kurokawa K, Ohba Y, Yoshizaki H, Mochizuki N, Matsuda M. 2002. Activation of Rac and Cdc42 Video Imaged by Fluorescent Resonance Energy Transfer-Based Single-Molecule Probes in the Membrane of Living Cells. *Mol Cell Biol* **22**:6582–6591. doi:10.1128/MCB.22.18.6582-6591.2002

Kaushik S, Ravi A, Hameed FM, Low BC. 2014. Concerted modulation of paxillin dynamics at focal adhesions by deleted in liver cancer-1 and focal adhesion kinase during early cell spreading: DLC1 Regulates Paxillin Dynamics at Focal Adhesions via FAK. *Cytoskeleton* **71**:677–694. doi:10.1002/cm.21201

Kraynov VS, Chamberlain C, Bokoch GM, Schwartz MA, Slabaugh S, Hahn KM. 2000. Localized Rac activation dynamics visualized in living cells. *Science* **290**:333–337.

Krendel M, Zenke FT, Bokoch GM. 2002. Nucleotide exchange factor GEF-H1 mediates cross-talk between microtubules and the actin cytoskeleton. *Nat Cell Biol* **4**:294–301. doi:10.1038/ncb773

Li G, Du X, Vass WC, Papageorge AG, Lowy DR, Qian X. 2011. Full activity of the deleted in liver cancer 1 (DLC1) tumor suppressor depends on an LD-like motif that binds talin and focal adhesion kinase (FAK). *Proc Natl Acad Sci* **108**:17129–17134. doi:10.1073/pnas.1112122108

Machacek M, Hodgson L, Welch C, Elliott H, Pertz O, Nalbant P, Abell A, Johnson GL, Hahn KM, Danuser G. 2009. Coordination of Rho GTPase activities during cell protrusion. *Nature* **461**:99–103. doi:10.1038/nature08242

Mahlandt EK, Arts JJG, van der Meer WJ, van der Linden FH, Tol S, van Buul JD, Gadella TWJ, Goedhart J. 2021. Visualizing endogenous Rho activity with an improved localization-based, genetically encoded biosensor. *J Cell Sci* **134**:jcs258823. doi:10.1242/jcs.258823

Martin K, Reimann A, Fritz RD, Ryu H, Jeon NL, Pertz O. 2016. Spatio-temporal co-ordination of RhoA, Rac1 and Cdc42 activation during prototypical edge protrusion and retraction dynamics. *Sci Rep* **6**:21901. doi:10.1038/srep21901

Martin K, Vilela M, Jeon NL, Danuser G, Pertz O. 2014. A growth factor-induced, spatially organizing cytoskeletal module enables rapid and persistent fibroblast migration. *Dev Cell* **30**:701–716. doi:10.1016/j.devcel.2014.07.022

Matasci M, Baldi L, Hacker DL, Wurm FM. 2011. The PiggyBac transposon enhances the frequency of CHO stable cell line generation and yields recombinant lines with superior productivity and stability. *Biotechnol Bioeng* **108**:2141–2150. doi:10.1002/bit.23167

Moon SY, Zheng Y. 2003. Rho GTPase-activating proteins in cell regulation. *Trends Cell Biol* **13**:13–22. doi:10.1016/s0962-8924(02)00004-1

Mosaddeghzadeh N, Ahmadian MR. 2021. The RHO Family GTPases: Mechanisms of Regulation and Signaling. *Cells* **10**:1831. doi:10.3390/cells10071831

Müller PM, Rademacher J, Bagshaw RD, Wortmann C, Barth C, van Unen J, Alp KM, Giudice G, Eccles RL, Heinrich LE, Pascual-Vargas P, Sanchez-Castro M, Brandenburg L, Mbamalu G, Tucholska M, Spatt L, Czajkowski MT, Welke R-W, Zhang S, Nguyen V, Rrustemi T, Trnka P, Freitag K, Larsen B, Popp O, Mertins P, Gingras A-C, Roth FP, Colwill K, Bakal C, Pertz O, Pawson T, Petsalaki E, Rocks O. 2020. Systems analysis of RhoGEF and RhoGAP regulatory proteins reveals spatially organized RAC1 signalling from integrin adhesions. *Nat Cell Biol* **22**:498–511. doi:10.1038/s41556-020-0488-x

Nalbant P, Hodgson L, Kraynov V, Toutchkine A, Hahn KM. 2004. Activation of endogenous Cdc42 visualized in living cells. *Science* **305**:1615–1619.

Natwick DE, Collins SR. 2021. Optimized iLID Membrane Anchors for Local Optogenetic Protein Recruitment. *ACS Synth Biol* **10**:1009–1023. doi:10.1021/acssynbio.0c00511

Oakes PW, Wagner E, Brand CA, Probst D, Linke M, Schwarz US, Glotzer M, Gardel ML. 2017. Optogenetic control of RhoA reveals zyxin-mediated elasticity of stress fibres. *Nat Commun* **8**:15817–12.

Pertz O. 2010. Spatio-temporal Rho GTPase signaling - where are we now? *J Cell Sci* **123**:1841–1850. doi:10.1242/jcs.064345

Pertz O, Hodgson L, Klemke RL, Hahn KM. 2006. Spatiotemporal dynamics of RhoA activity in migrating cells. *Nature* **440**:1069–1072. doi:10.1038/nature04665

Riedl J, Crevenna AH, Kessenbrock K, Yu JH, Neukirchen D, Bista M, Bradke F, Jenne D, Holak TA, Werb Z, Sixt M, Wedlich-Soldner R. 2008. Lifeact: a versatile marker to visualize F-actin. *Nat Methods* **5**:605–607. doi:10.1038/nmeth.1220

Rossman KL, Der CJ, Sondek J. 2005. GEF means go: turning on RHO GTPases with guanine nucleotide-exchange factors. *Nat Rev Mol Cell Biol* **6**:167–180.

Ryu H, Chung M, Dobrzyński M, Fey D, Blum Y, Lee SS, Peter M, Kholodenko BN, Jeon NL, Pertz O. 2015. Frequency modulation of ERK activation dynamics rewires cell fate. *Mol Syst Biol* **11**:838. doi:10.15252/msb.20156458

Schindelin J, Arganda-Carreras I, Frise E, Kaynig V, Longair M, Pietzsch T, Preibisch S, Rueden C, Saalfeld S, Schmid B, Tinevez J-Y, White DJ, Hartenstein V, Eliceiri K, Tomancak P, Cardona A. 2012. Fiji: an open-source platform for biological-image analysis. *Nat Methods* **9**:676–682. doi:10.1038/nmeth.2019

Schmick M, Kraemer A, Bastiaens PIH. 2015. Ras moves to stay in place. *Trends Cell Biol* **25**:190–197.

Tsyganov MA, Kolch W, Kholodenko BN. 2012. The topology design principles that determine the spatiotemporal dynamics of G-protein cascades. *Mol Biosyst* **8**:730–743.

Wu C-F, Lew DJ. 2013. Beyond Symmetry Breaking: Competition and Negative Feedback in GTPase regulation. *Trends Cell Biol* **23**:476–483. doi:10.1016/j.tcb.2013.05.003

Zhao Y, Lykov N, Tzeng C. 2022. Talin-1 interaction network in cellular mechanotransduction (Review). *Int J Mol Med* **49**:1–12. doi:10.3892/ijmm.2022.5116

Figure 1. Cytoskeletal structures in WT and DLC1 deficient cells.

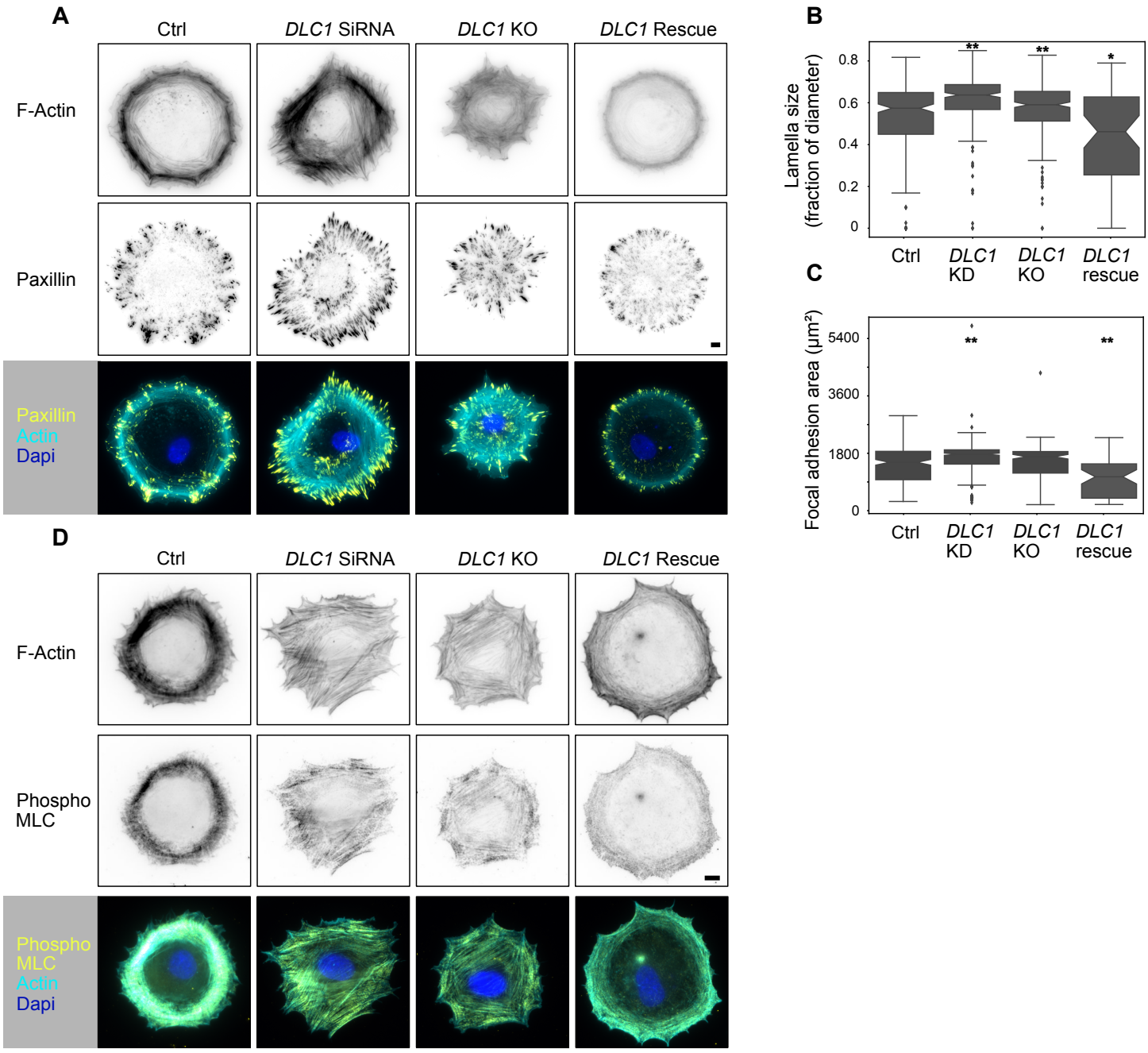

Figure 2. F-actin dynamics and cell morphodynamics in WT and DLC1 KO cells.

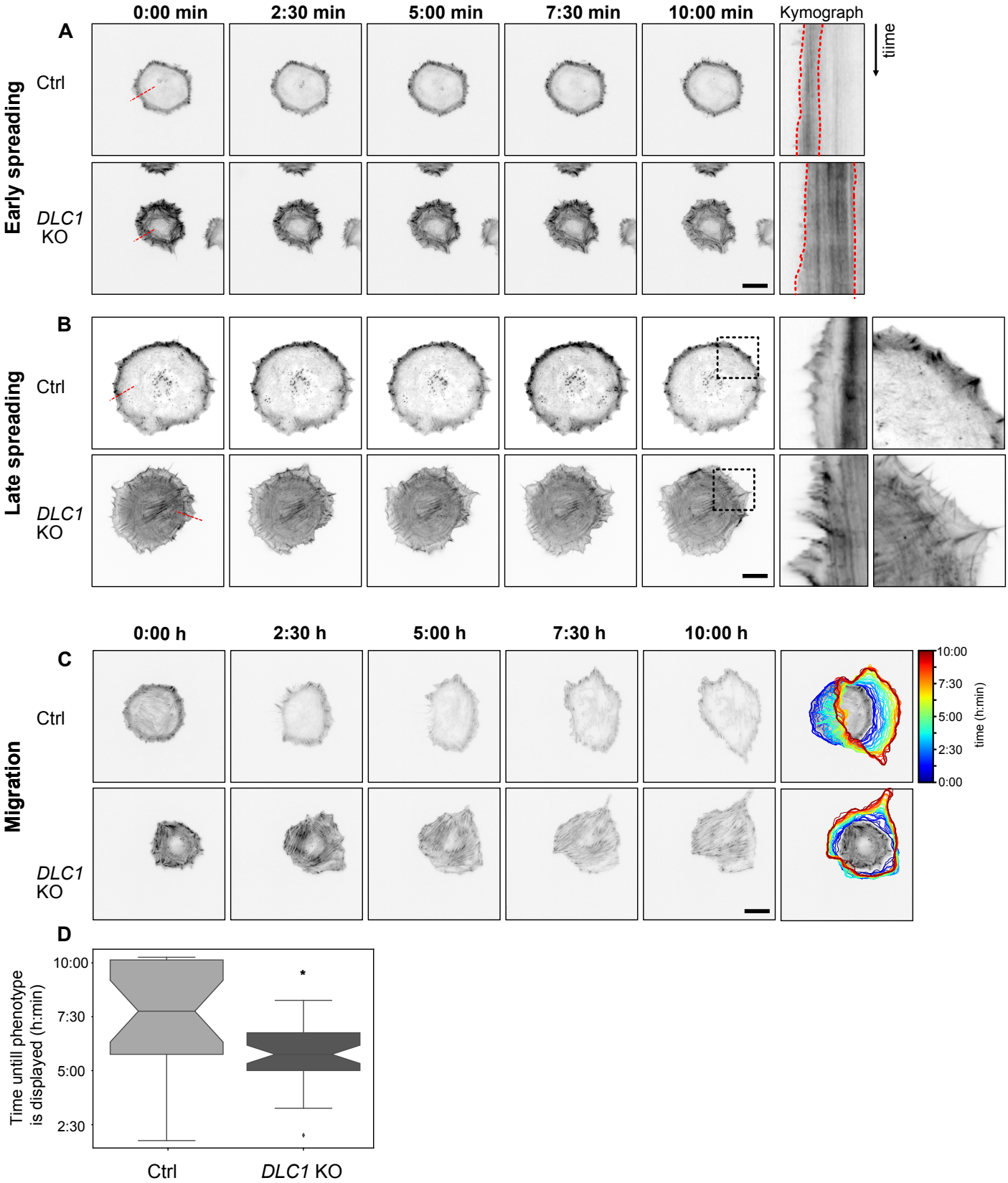

Figure 3. RhoA activation dynamics in WT and DLC1 KO cells

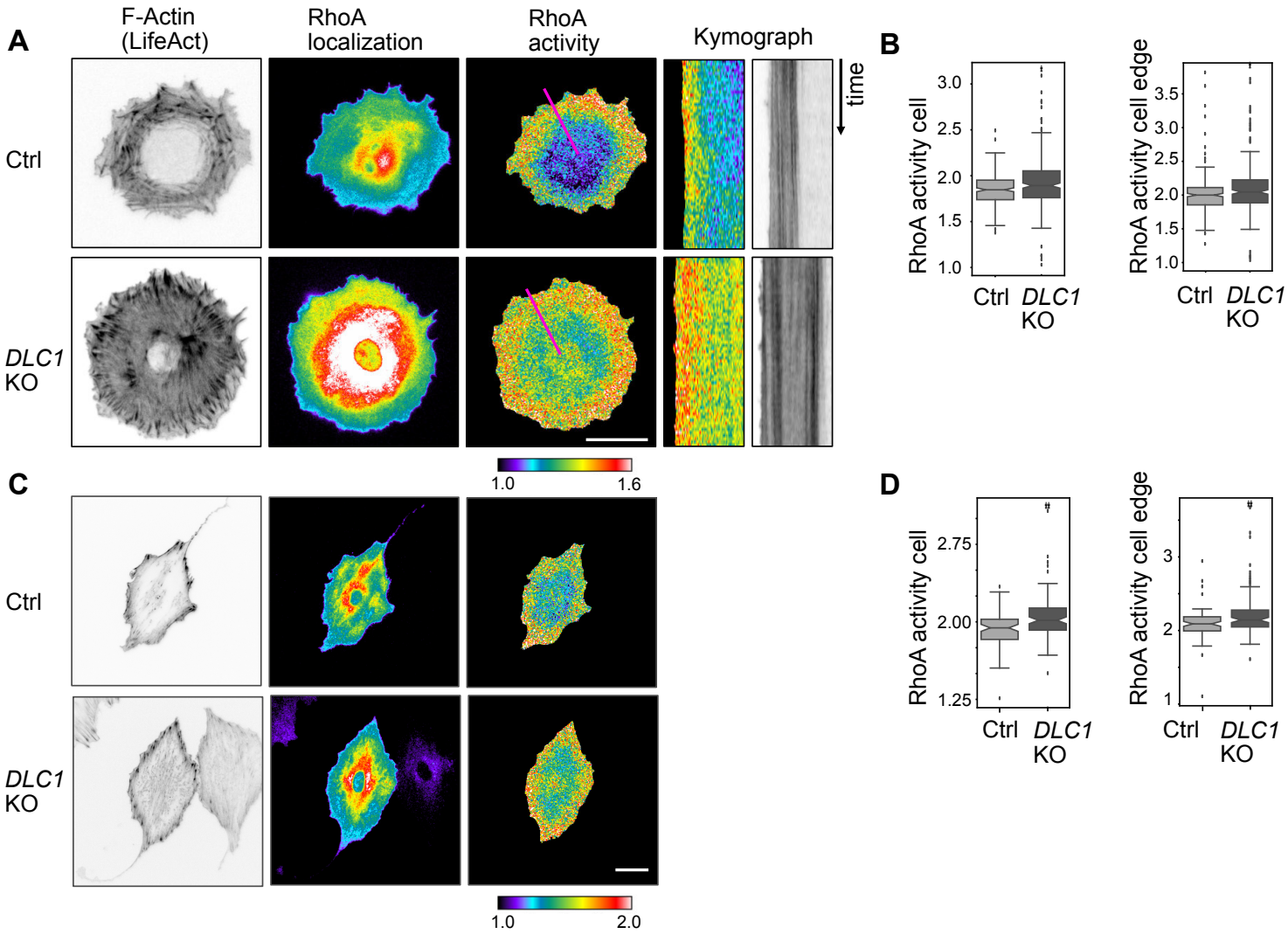

Figure 4. An optogenetic actuator- Rho biosensor circuit to probe Rho GTPase flux

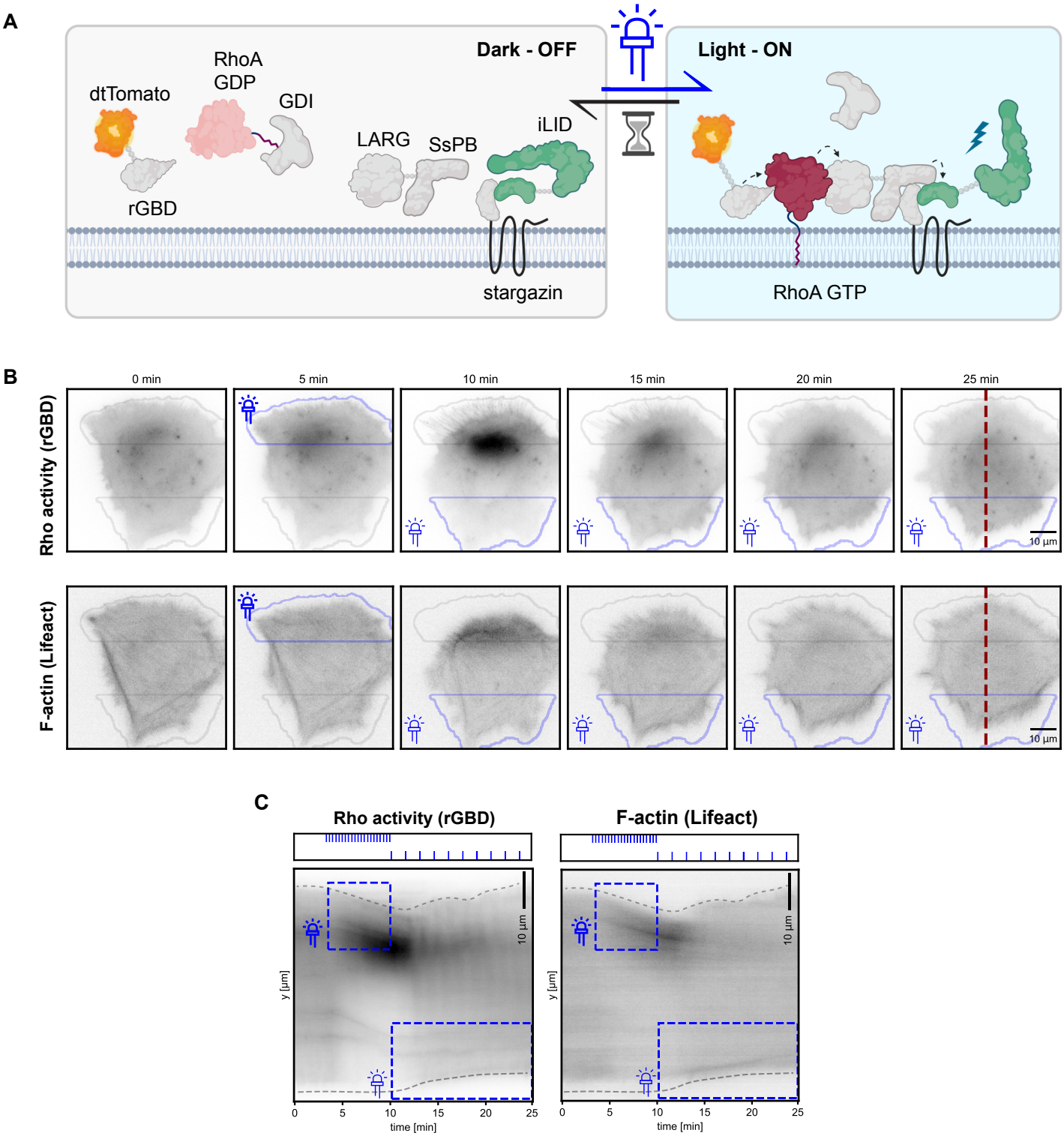

Figure 5. Rho GTPase activation kinetics in WT versus DLC1 KO cells

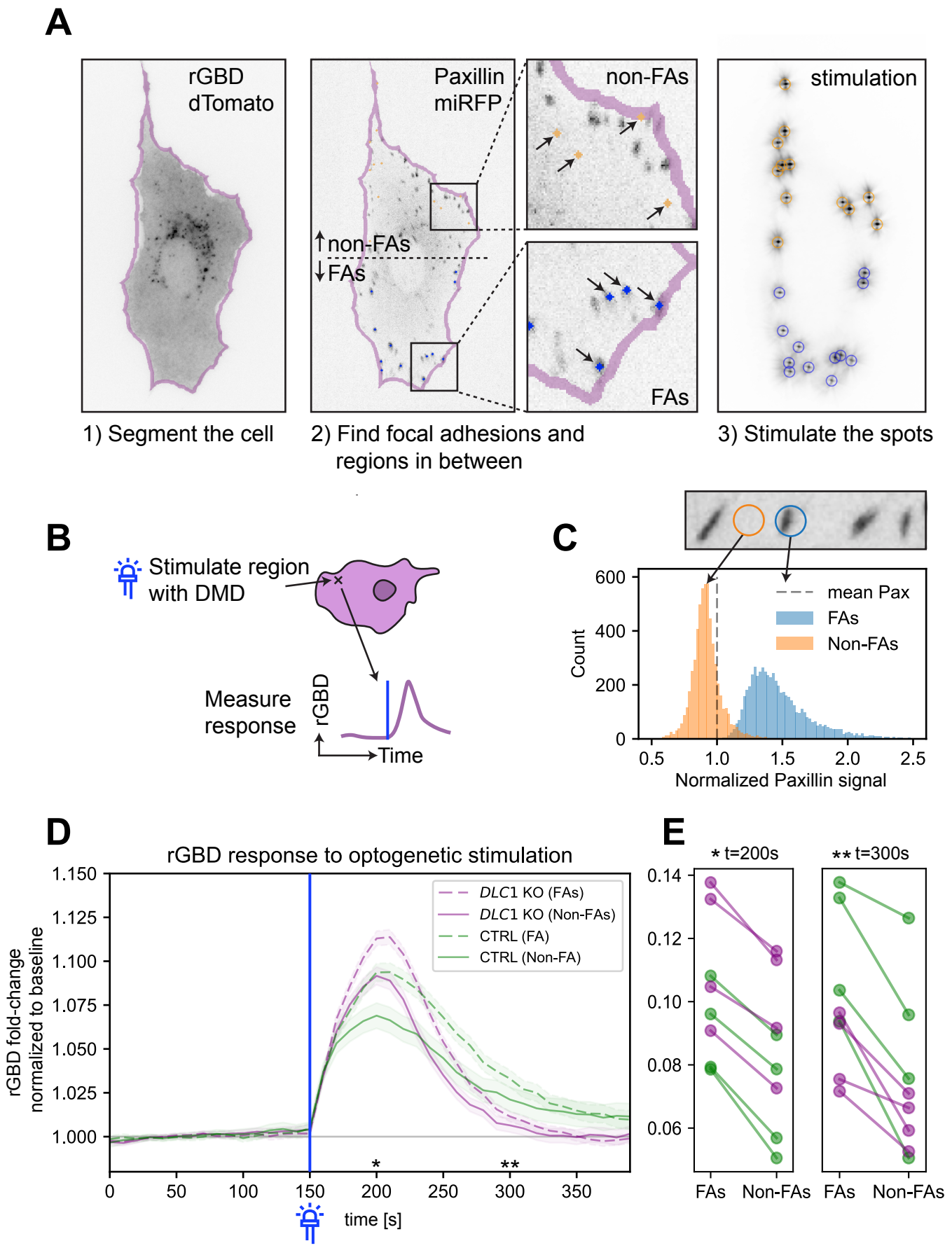

Figure 6. Optogenetic control of force-dependent DLC1 interactions with Fas

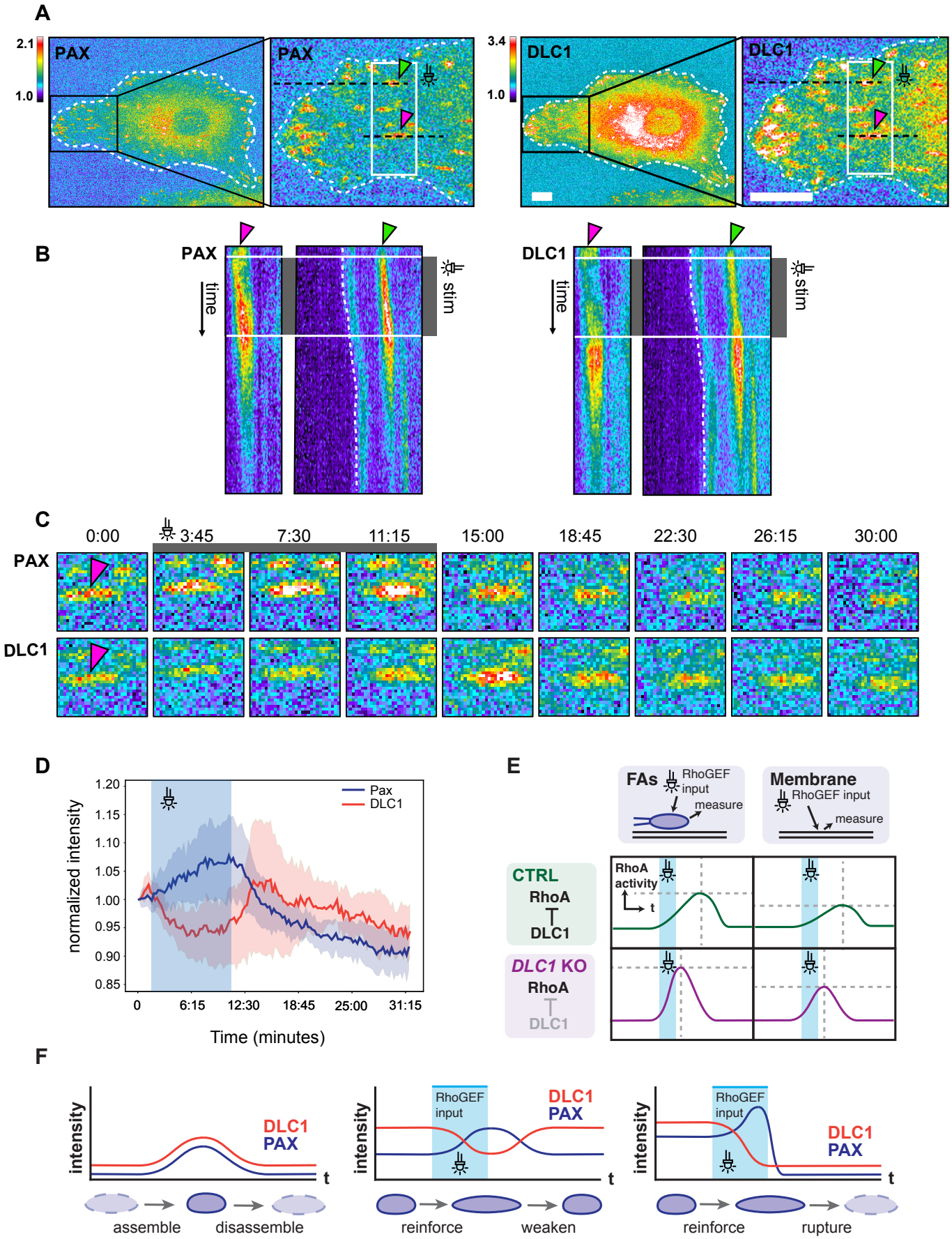

Figure S1: Cell motility properties in WT versus DLC1 KO cells

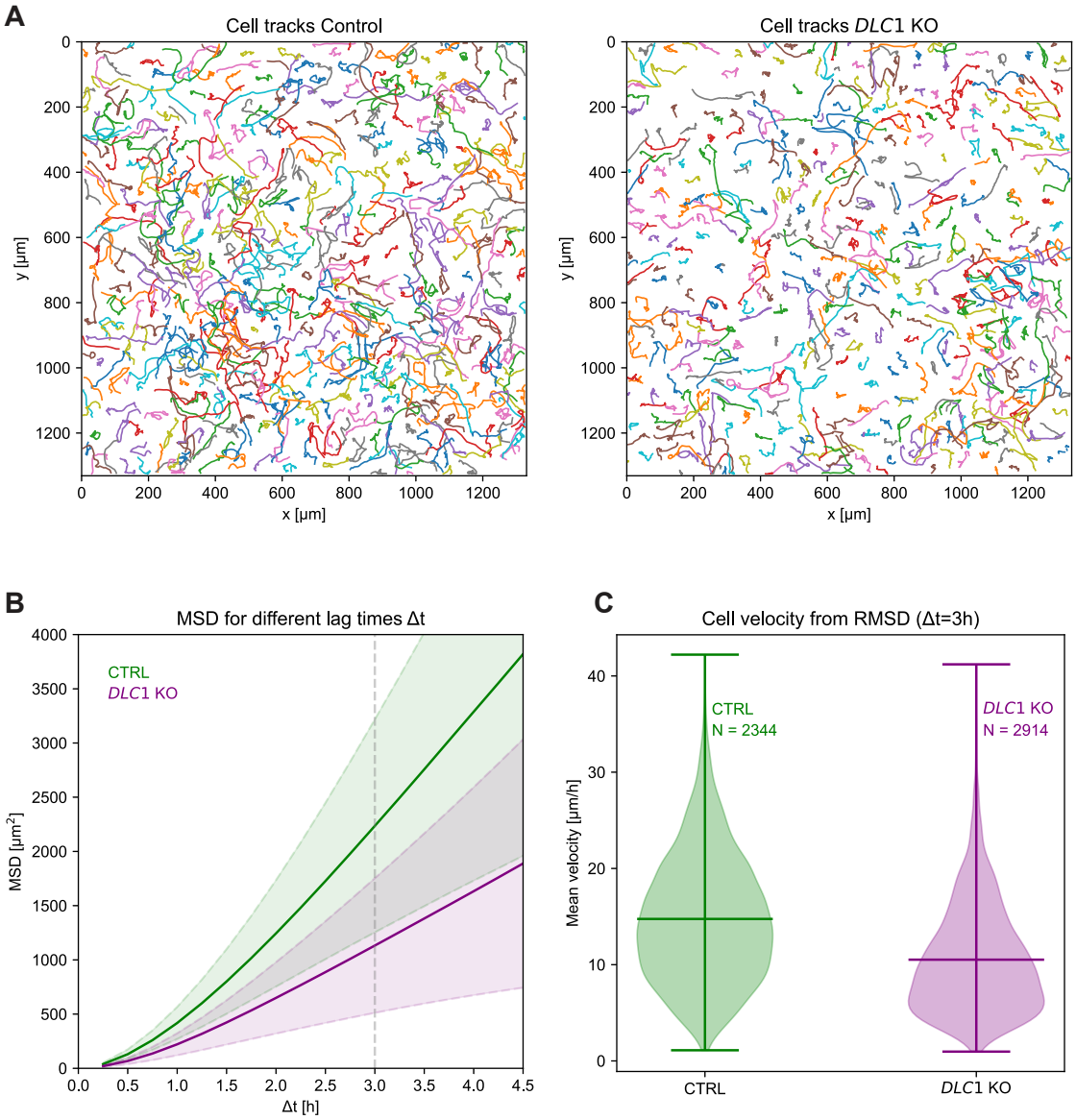

Figure S2. Effect of DLC1 overexpression on F-actin cytoskeleton and RhoA activity

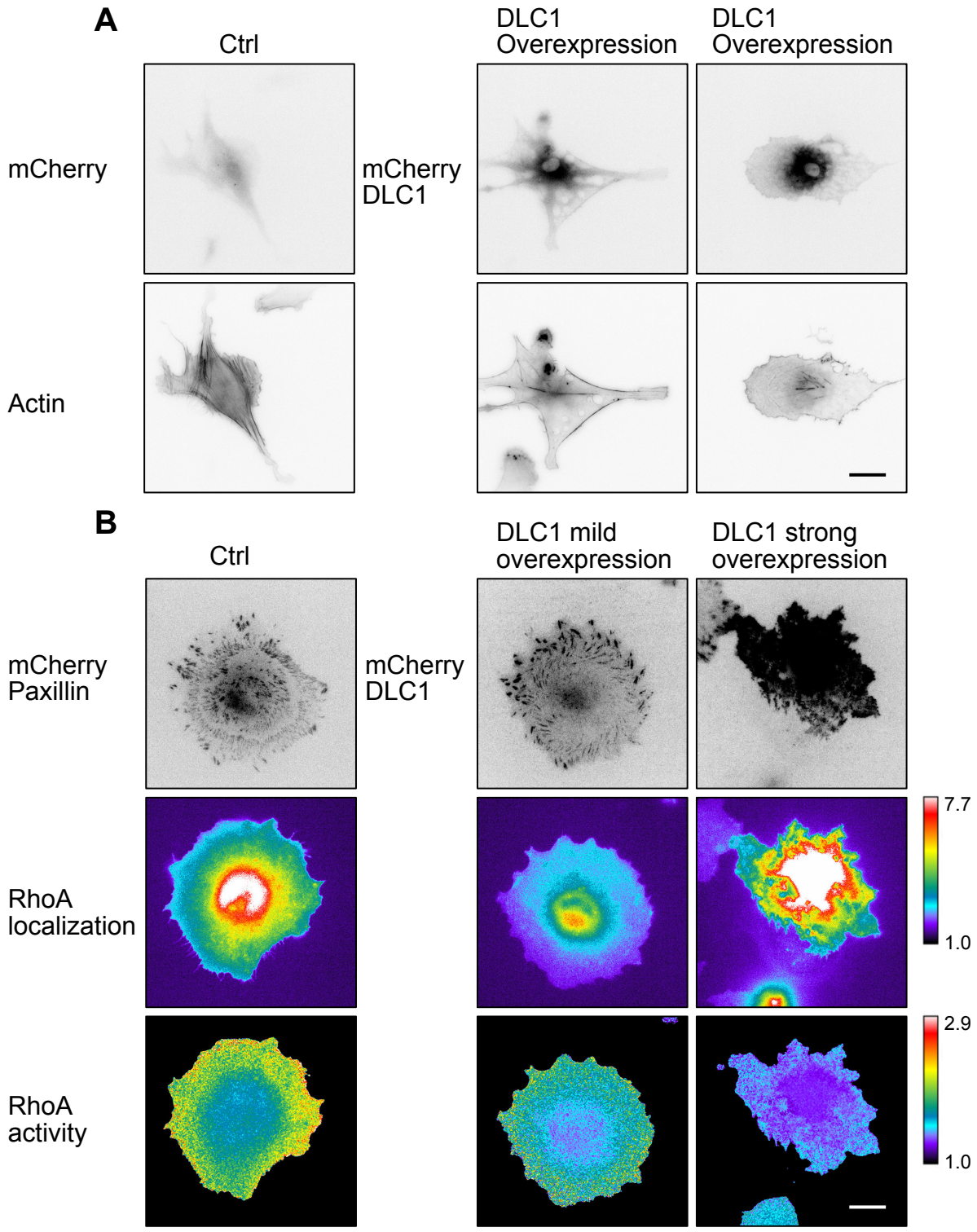

Figure S3. DLC1 dynamics at FAs in unperturbed cells

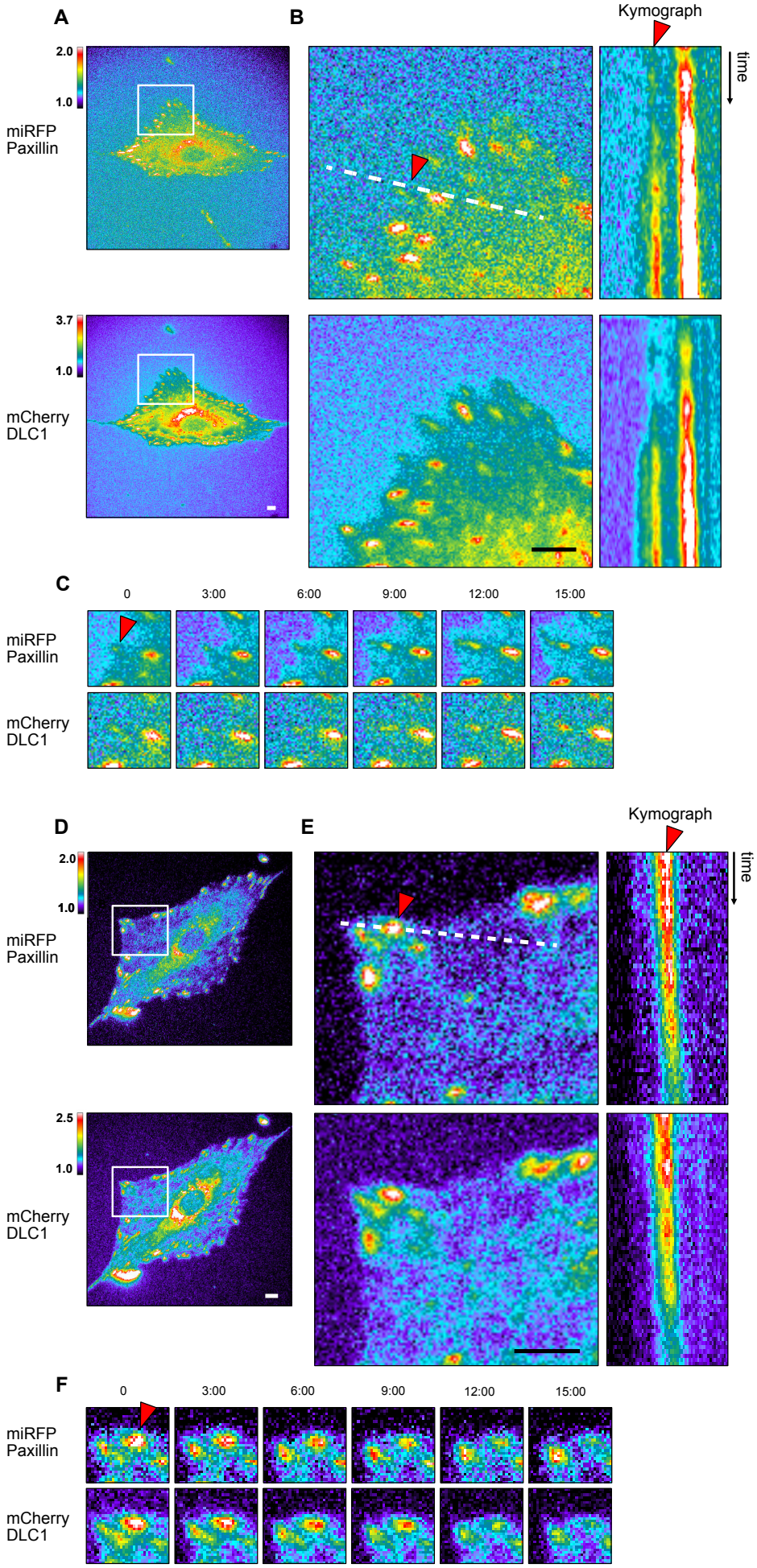
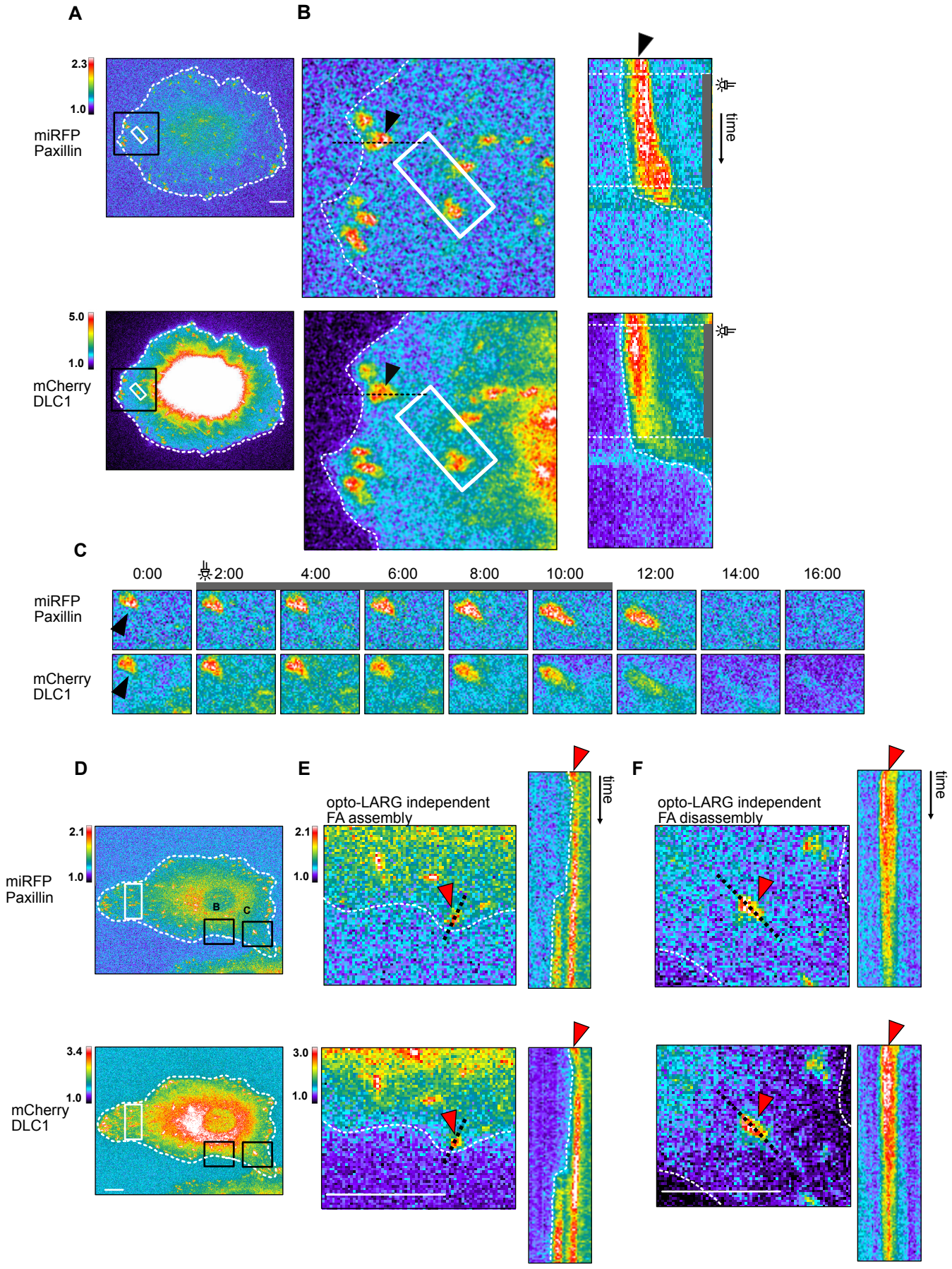
Figure S4. DLC1 dynamics in an optoLARG stimulated FA that undergoes reinforcement followed by disassembly, as well as FA behavior in absence of optoLARG stimulus